THESIS

A LAGRANGIAN PERSPECTIVE ON DEEP CONVECTIVE TROPICAL RAINING SYSTEMS

Submitted by

David Ian Duncan

Department of Atmospheric Science

In partial fulfillment of the requirements

For the Degree of Master of Science

Colorado State University

Fort Collins, Colorado

Spring 2013

Master's Committee:

Advisor: Christian D. Kummerow

David W. J. Thompson
Steven C. Reising

ABSTRACT

A LAGRANGIAN PERSPECTIVE ON DEEP CONVECTIVE TROPICAL RAINING SYSTEMS

Deep convective precipitating systems are categorized, tracked, and analyzed in the Tropical Ocean. Precipitating systems are tracked via an algorithm applied to the high-resolution CPC Morphing technique (CMORPH) precipitation product. Systems are categorized with an objective method, using data from the Tropical Rainfall Measuring Mission (TRMM) Microwave Imager (TMI) and a K-means clustering algorithm that exploits the consistency and similarity of tropical precipitation regimes. Propagation characteristics of these systems are found to be remarkably similar among ocean basins. The raining system's geographic center is calculated at each time step, allowing various ancillary datasets to be co-located with these systems to permit analysis of the effect of deep convective raining systems on local oceanic environments. The ancillary fields examined comprise elements of the water and energy budgets, as well as cloud field information from the International Satellite Cloud Climatology Project (ISCCP).

The biggest determinant of a system's environmental impact is its propagation speed. This finding is corroborated by analysis of cloud fields which show that slow-moving systems and their associated deep clouds persist longer in a given location and therefore have a greater impact on the local environment than systems that move through more quickly. In the mean, sea surface temperature (SST) drops by 0.1-0.3°C and total precipitable water (TPW) increases by 5-7kg/m^2 due to the passage of a deep convective raining system, with impacts dependent on the ocean basin and system speed. The presence of pervasive, optically thick clouds greatly decreases the net radiative flux at the surface, acting as the key driver of the observed drop in SST. The existence of a possible precipitation feedback based on system propagation speed is also explored.

ACKNOWLEDGEMENTS

The work presented here would not have been possible without a great deal of generous support. First and foremost, I thank my advisor, Chris Kummerow, for his guidance, support, and imbuing me with a sense of how science and research should be conducted. I extend my gratitude to Drs. Dave Thompson and Steve Reising for serving on my master's committee. I would like to thank the entire Kummerow research group for support and camaraderie throughout my time in Fort Collins. I would especially like to thank Dr. Greg Elsaesser, a surrogate advisor of sorts, and Josh King, my officemate, for being highly valuable sounding boards for many research ideas. My colleagues and the faculty at the Colorado State University Department of Atmospheric Science have aided in my growth as a scientist, and I am grateful to be a part of this elite group. I express deep thanks to my parents for supporting my education in innumerable ways over many years. Thank you to anyone who has ever taught me anything or challenged my perception of the world around me. This work was supported by grants from the National Aeronautics and Space Administration, MEaSUREs (Making Earth System Data Records for Use in Research Environments) grant NNX08AT04A and PMM (Precipitation Measurement Mission) grant NNX10AG75G.

TABLE OF CONTENTS

ABSTRACT ii
ACKNOWLEDGEMENTS iv
TABLE OF CONTENTS v

SECTION 1: INTRODUCTION 1
  1.1 Motivation 1
  1.2 Microwave remote sensing 6
  1.3 Mesoscale convective systems 9
    1.3.1 Importance 9
    1.3.2 Classification 10
  1.4 Previous studies 11
  1.5 Overview 13
SECTION 2: DATA SETS 16
  2.1 TRMM Microwave Imager and GProf 16
  2.2 Precipitation Radar 17
  2.3 Cloud regimes 18
  2.4 State variables 21
    2.4.1 SeaFlux 21
    2.4.2 ECMWF Interim Reanalysis 22
    2.4.3 Surface Radiation Budget 24
    2.4.4 Global Tropical Moored Buoy Array 25
SECTION 3: METHODS 26
  3.1 Tracking 26
  3.2 Categorization 31
    3.2.1 Motivation and background 31
    3.2.2 Technical aspects 32
    3.2.3 Statistical foundation 35
    3.2.4 Consistency and similarity 37
SECTION 4: ENVIRONMENT 40
  4.1 Introduction 40
  4.2 Clouds 41
  4.3 Shear 45
  4.4 Water vapor 46
  4.5 Evaporation 51
  4.6 Water vapor convergence 53
  4.7 Sea surface temperature 55
  4.8 Radiative fluxes 61
SECTION 5: FEEDBACKS 67
  5.1 Introduction 67
  5.2 Rain rate feedback 68
SECTION 6: SUMMARY 76
REFERENCES 78
APPENDIX 83

1. INTRODUCTION

1.1 Motivation

Global precipitation is inextricably linked to Earth's radiative energy balance. Incoming solar radiation at the top of the atmosphere is both reflected back as well as absorbed by the atmosphere and the Earth's surface. Some of the absorbed radiation is reemitted as longwave radiation from clouds or the Earth's surface. To retain radiative balance at the Earth's surface and in the atmosphere, excess energy at the surface caused by these radiative fluxes is transported up into the atmosphere via sensible and latent heat. This is required by the dictates of radiative-convective equilibrium: the rate at which temperature decreases with altitude in the troposphere determines atmospheric stability, which provides a mechanism to transport moisture into the atmosphere, thus restoring stability whenever the surface is not in radiative balance. Global evaporation is thereby constrained to keep the atmosphere in balance by way of latent heat release, linking the planet's hydrologic cycle to the budget of radiative energy. The atmosphere has a very limited capacity to store water, requiring that all of the water that condenses to satisfy the energy budget be precipitated out in a short period of time. Global precipitation is therefore required to match global evaporation, connecting precipitation to the atmospheric energy budget.

Due to the fact that evaporation is equal to precipitation on a global scale, one should be calculable by determining the other. With evaporative energy (latent heat) being difficult to measure directly on large scales, it can be computed as a residual from the surface radiation budget, or it can be calculated via bulk formulae. However, radiative estimates do not agree very well with precipitation estimates. The best estimate of precipitation biases from a widely vetted and respected data record, the Global Precipitation Climatology Project, is that global precipitation averages 2.6mm/day ±9% (hereafter GPCP; Adler et al. 2012). The GPCP data record is largely dependent on satellite estimates of rainfall, from both microwave and infrared instruments, but also uses a network of rain gauge data over land (Adler et al. 2003). From a large synthesis study by Trenberth et al. (2009), global evaporation is estimated to be 80W/m^2. By simple calculation, this equates to an evaporation rate of 2.8mm/day, a value 7% higher than the global precipitation rate given by GPCP. Other studies, such as Wild (2012) and Stephens et al. (2012) consider that to be an underestimate. After factoring in recent data from the CloudSat mission that claims longwave downward radiation from the atmosphere is 20W/m^2 higher than quoted in the 4th IPCC report (Meehl et al. 2007), the radiation budget is massaged by decreasing shortwave radiation absorbed by the surface and increasing evaporation to 88W/m^2, equating to 3.08mm/day of precipitation (Stephens et al. 2012).

This discrepancy between two observations that should match is unsettling; it is impossible to claim a full understanding of the global water and energy cycles when the observational energy budget does not close. To put it into perspective, this difference in estimates is an order of magnitude larger than current estimates of the net radiant flux into the surface that is causing the planet to warm (Trenberth et al. 2009). This difference, 2.6mm/day from GPCP versus 3.08mm/day from recent energy balance studies, suggests that there is 0.48mm/day of precipitation missing, equating to 17cm of missing precipitation annually on a global average.

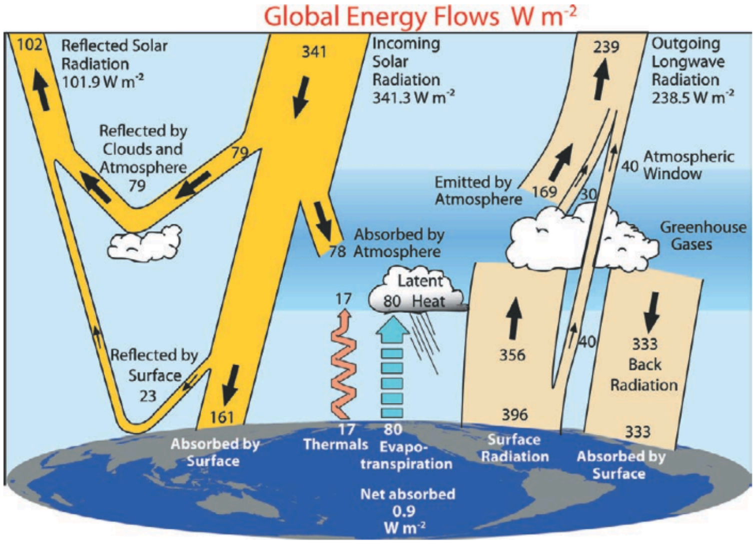

Figure 1.1. A view of the global energy balance, from Trenberth et al. (2009).

With all of the concern regarding climate change, trends in climatological datasets carry deep importance. Numerous studies and state of the art climate models predict increased atmospheric water vapor and a more vigorous hydrologic cycle as the Earth warms; models predict an increase in total atmospheric water content of 7%/K of warming, and a muted 1-3%/K increase in total rainfall (Held and Soden 2006). The volatility and length of the satellite-based observational record make definitive statements about global trends in global precipitation difficult. Wentz et al. (2007) found positive trends in precipitation, evaporation, and total precipitable water (TPW) from 1987 to 2006, showing a 6%/K increase in rainfall due to the planet's warming.

In contrast, instead of seeing an increase in global precipitation as predicted, analysis of the GPCP record shows no discernible trend whatsoever from 1978 through 2011. There was a slight positive trend of 0.0078 mm/day/decade up through 2005 (Gu et al. 2007), but with data up through mid 2011 the trend is now almost completely flat at -0.002 mm/year/decade. The very small changes expected are of a greater magnitude than the overall biases in the data records, making it difficult to reach any firm conclusions about climatological trends in precipitation.

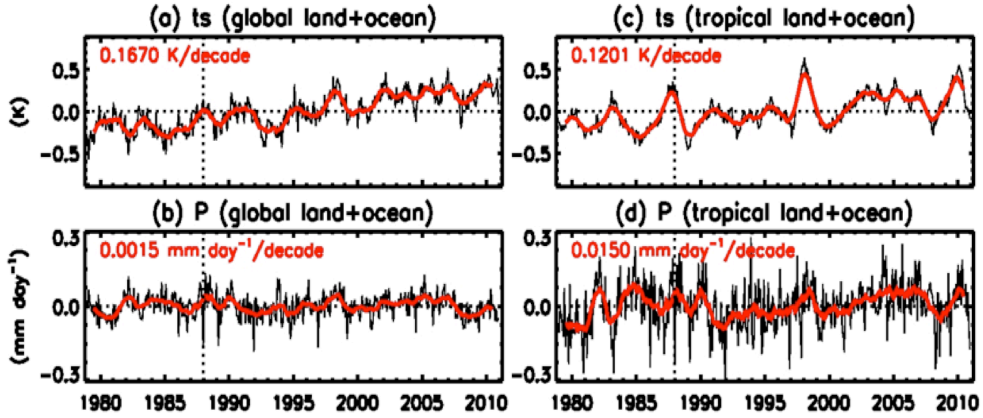

Figure 1.2. Surface temperature (a,c) and precipitation trends from GPCP (b,d), courtesy personal communication.

It is likely that both the retrieval methods and the climate models have errors. It is also possible that the nature of precipitation is changing and retrieval algorithms are not sensitive to this change; or that the theory and mechanics embedded in the models do not accurately reflect what is truly happening in the natural world. Numerous studies argue the latter, especially regarding intraseasonal (Soden 2000) and decadal variability of rainfall in climate models (Wentz et al. 2007). Retrieval algorithms have also been shown many times to be quite sensitive to certain changes. Recorded instances in the literature include a great sensitivity to changes in tropical sea surface temperature (Lau and Wu 2011; Berg et al. 2006).

The problems facing microwave retrievals and climate models arise from a lack of information. Climate models can only be as good as accumulated knowledge and parameterizations allow them; the difficulties inherent in satellite retrievals are caused by the 'underconstrained' nature of the problem—too many variables to solve for and not enough information (Stephens and Kummerow 2007). Given perfect knowledge and a worthy retrieval, or infinite resolution and perfect parameterizations, satellite-estimated rainfall and climate models could theoretically be in complete agreement. The latest generation of microwave sensors for the remote sensing of precipitation, namely the Global Precipitation Measurement (GPM) mission, will attempt to add further information by way of a dual frequency radar. If successful, it will reduce uncertainties, but not eliminate them altogether.

A key feature of consensus between climate models is that areas of the Tropics will receive more precipitation while the subtropics will generally dry out (Meehl et al. 2007). Intense rain in the Tropics accounts for large fractions of total precipitation, and is expected to increase in a warming climate. However, the current skill in modeling intense precipitation especially in the Tropics is 'dreary' (Stephens et al. 2010), as convective parameterizations do not recreate the most extreme rain rates and therefore miss some salient features of the hydrologic cycle.

One way to add information that can profit both models and retrievals is to gain a deeper understanding of the individual units that produce most of the heavy precipitation in the Tropics, mesoscale convective systems (MCSs). One study estimated that as much as 70-80% of precipitation in the Tropics comes from MCSs (Mohr et al. (1999)). Most observations of MCS activity in the Tropics come from orbiting satellite instruments, which provide snapshots of the environment but no information on the temporal variability of a scene. This limitation, combined with the fact that an MCS can propagate hundreds of kilometers and last for hours or days, makes analysis of discrete raining systems difficult. Systems should be examined individually to analyze their characteristics and impact on the environment in which they occur. Moreover, since an MCS and its associated cloud field is never completely stationary, analyzing its behavior from a stationary framework is a major limitation overcome only by following individual systems. Ideally, with general characteristics of the MCS lifecycle better understood, this knowledge can be applied to improve retrievals and models.

1.2 Microwave remote sensing

Remote sensing of precipitation by passive microwave sensors is a vital constituent in the current makeup of efforts to observe global atmospheric behavior. Microwave radiometers compose a large number of the orbiting instruments that observe precipitation, providing valuable data on a global scale for multiple decades. Since the tracking and system categorization methods used in this study both rely upon rainfall data from passive microwave data, it is worth providing a brief overview of microwave remote sensing as it pertains to this study.

Since the first satellite radiometer was launched in 1959, microwave measurements from space have become an indispensible part of international efforts to observe the planet. Starting with the introduction of the Special Sensor Microwave/Imager (SSM/I) in the late 1980's, there has now been a fairly consistent passive microwave data record for the past 25 years. Newer instruments such as the TRMM (Tropical Rainfall Measuring Mission) Microwave Imager (TMI), Advanced Microwave Scanning Radiometer-EOS (AMSR-E), and the SSM/I successor, Special Sensor Microwave Imager/Sounder (SSMIS), continue this data record and are used for operational and research applications. The TMI instrument aboard TRMM, upon which much of this study relies, has been in orbit and providing data since late 1997 and is still operational as of 2013; it is the longest surviving microwave instrument ever used in orbit, offering a data record of unprecedented length.

The underlying foundation of microwave remote sensing is that all objects in the universe emit radiation of varying frequencies and intensities depending upon their temperature and emissivity. Matter with an emissivity of exactly one is termed a black body and emits radiation according to the Stefan-Boltzmann law, which states that the emission spectrum of a black body is directly proportional to its temperature to the fourth power (Peixoto and Oort 1992). Since the emissivities of common elements and compounds are well known, the temperature of most matter can be determined by sensing its black body radiance. Satellite radiometers are passive instruments, meaning that they simply measure incident radiation; active instruments, such as Radar, send out a signal and measure the signal that is returned.

Given the principles of black body radiation, the radiance data obtained by a passive microwave sensor can be used to calculate a brightness temperature (T_b), the corresponding temperature of a black body emitting at that particular intensity. It is then brightness temperatures, discrete in space and time, which are input to algorithms in order to calculate many variables including the rain rate. Microwave instruments currently in orbit employ multiple frequencies, or channels, to gather as much data on the state of the atmosphere as possible. For example, the TMI instrument has nine channels ranging in frequency from 10.65-85.5GHz, with both vertically and horizontally polarized channels at 10.65, 19.35, 37.0, and 85.5GHz (Kummerow et al. 1998). The 21.3GHz channel is important for the observation of water vapor, as vapor is strongly attenuating at that frequency. Part of the reason why microwave remote sensing is widely used is that clouds are relatively transparent in the portion of the microwave spectrum used, allowing the surface to be measured and hydrometeors to stand out.

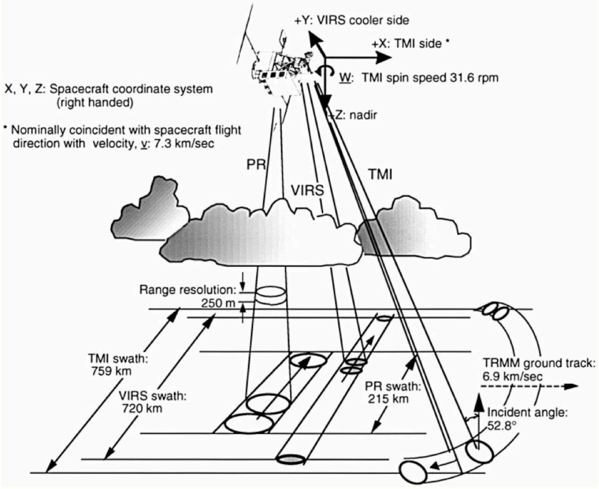

Figure 1.3. Schematic of TMI and PR instruments' swaths as the TRMM satellite orbits. From Kummerow et al. 1998.

Raw brightness temperatures, however, are not very useful to determine anything specific without the use of a retrieval algorithm. The retrieval algorithm used in this study is the Goddard Profiling algorithm 2010 version 1 (hereafter Gprof; Kummerow et al. 2011). The current version of GProf uses a radiative transfer model, a Bayesian retrieval, and an a priori database of cloud-resolving model data matched with the TRMM Precipitation Radar to turn brightness temperatures into vertical profiles of hydrometeors and a host of other variables. One advantage of recent versions of GProf is that it computes rainfall separated into stratiform and convective portions, an element utilized in this study when placing raining scenes into various regime types.

Remote sensing in the microwave spectrum depends upon knowledge of the Earth's surface. Without accurate information as to the temperature and emissivity of the surface, it is unclear as to whether or not certain channels are viewing the surface or an object just above the surface, such as low cloud cover. This issue is fairly easily resolved over water, as there are highly accurate measurements of sea surface temperature (SST) readily available and the emissivity of seawater is well known (Reynolds et al. 2007). Unfortunately, the emissivity of land surfaces can change quickly and markedly due to changes in soil moisture, vegetation, fraction covered by water, and numerous other factors; microwave retrievals over land are thus far quite inferior to retrievals over ocean. This study will focus solely on scenes that are 100% ocean.

This proficiency at observing precipitation over water, coupled with the modern proliferation of passive microwave instruments in orbit, has made the global ocean an ideal area of study for the remote sensing of precipitation. With high accuracy and improving spatiotemporal coverage, remote sensing of the Tropics offers a rich trove of data and thus much room for research. As mentioned previously, the next generation of precipitation remote sensing, GPM, will build upon the successes of microwave instruments of the past few decades. Its stated goal is to provide measurements of precipitation all over the globe every 2-4 hours, utilizing a constellation of radiometers and a core observatory satellite to which all other radiometers are calibrated.

1.3 Tropical mesoscale convective systems

1.3.1 Importance

A standard definition of a mesoscale convective system is a cloud system with both convective and stratiform regions, containing a vertical circulation driven by convective overturning that produces a contiguous precipitation area at least 100km wide in one dimension (Houze 1989). The systems that deposit the largest amounts of tropical rainfall contain regions of deep convection alongside mesoscale areas of stratiform precipitation, with the convective towers and anvil reaching near the tropopause while the stratiform cloud exists in the mid-troposphere. Ice and graupel particles are forced up by the convective flow with some particles detrained and advected into the stratiform cloud before melting and raining out. The heaviest rainfall occurs near the areas of strongest convection, while the stratiform areas cause lighter rainfall, with some drops evaporating before reaching the surface.

The focus of this study is deep convective MCSs in the Tropical Ocean. Deep convective precipitating systems in the Tropics transport vast amounts of water and energy in the Earth-atmosphere system. A thorough understanding of these systems is thereby crucial to any full conception of global water and energy budgets. Around three-quarters of the heat energy that the global atmosphere receives is from latent heat release through precipitation processes (Kummerow et al. 2000); 55% of total oceanic precipitation falls between 30°N and 30°S, with almost 40% of the total lying between 15°N and 15°S. Precipitation in the Tropics thereby accounts for nearly half of global atmospheric heating. Tropical MCSs can be short-lived or last for multiple days, remain fairly stationary or travel hundreds of kilometers, and span sizes that range from around 1000km^2 to bordering on the synoptic scale. The dynamical cause of many MCSs in the tropical ocean comes from various types of wave disturbances that include synoptic scale disturbances such as the Madden-Julian Oscillation (MJO; Madden and Julian 1972), easterly waves and convectively coupled Kelvin waves, or smaller-scale disturbances such as inertia-gravity waves (Tulich and Kiladis 2012). This study does not investigate the large-scale atmospheric dynamics that force MCS behavior and determine intensity and propagation characteristics. Other studies have examined convection and associated wave disturbances in the Tropics; this study focuses on the effects of these systems and not the causes.

1.3.2 Classification

To analyze deep convective MCS behavior, one first needs a way to systematically and objectively classify these systems. In Elsaesser et al. (2010), a K-means clustering method of classifying precipitating systems is used at the scale of approximately 1°x1° in the tropical ocean. That study found that scenes of tropical precipitation could be grouped into three distinct regimes: shallow, unorganized convection, and deep organized convection. This approach to categorizing precipitation recalls the trimodal characteristics of tropical convection in Johnson et al. (1999). The regimes found by Elsaesser et al. (2010) have distinct characteristics that are largely independent of location with heating profiles and rainfall distributions that are strikingly similar and consistent. This characteristic of ‘self-similarity’ therefore appears to constitute a good way to separate the study of deep convective MCS behavior from that of other precipitating systems in the Tropics. The objective classification in that study used space-borne radar data from the TRMM Precipitation Radar (PR).

This study endeavors to create a classification system similar to that used in Elsaesser et al. (2010), instead using passive microwave sources and thereby increasing possible coverage of the Tropics in both time and space. To augment this approach, precipitation data from CMORPH (Climate Prediction Center Morphing technique) is used to provide .25°x.25° coverage of the entire Tropics at three-hour intervals (Joyce et al. 2004). The CMORPH data set has been proven a state-of-the-art rainfall product, correlating very well with gauge data and outperforming similar rainfall products (Sapiano and Arkin 2009). Over oceans, CMORPH uses passive microwave precipitation estimates exclusively, employing all available microwave instruments in orbit from 2003 to the present; TMI and AMSR-E both employ the GProf retrieval operationally to provide rain rates, and are two of the instruments whose data is assimilated into the CMORPH product. Using this gridded product, an algorithm for tracking systems is developed, applied to all ocean basins spanning the tropics, joining contiguous CMORPH pixels into cohesive precipitation systems and tracing their movement through space and time. With this breadth of information, precipitating systems in the Tropics can be classified and tracked, allowing a complete picture of mean behavior to emerge. More specific details regarding the methods for classification and tracking of raining systems are to be found in Section 3.

1.4 Previous studies

Presented here are a few examples of studies that have also tracked tropical precipitating systems or looked at mesoscale cloud and precipitation structures. Each uses a slightly different method, and while they analyze diverse topics that are not necessarily the same as those explored here, they provide valuable background and contrast.

Wheeler and Kiladis (1999) uses outgoing longwave radiation (OLR) as a proxy for tracking deep convection, taking nearly two decades of satellite data to conduct spectral analysis in order to find mean wave behavior. That particular study is concerned with the large-scale dynamics and types of waves that drive the observed spectral peaks, rather than precipitation characteristics. Wheeler and Kiladis (1999) include OLR disturbances over land as well as ocean, producing a climatology of convectively coupled equatorial waves from 15°N-15°S.

Dias et al. (2012) takes direct brightness temperatures (T_bs) from a 3-hourly 0.5°x0.5° grid and assesses deep convection based upon a range of T_b thresholds. The dataset used to determine these "contiguous cloud regions" is the Cloud Archive User Services dataset, which contains 23 years of gridded brightness temperatures. Their "object-based" method requires systems to be propagating, fall within 15°N-15°S, and be contiguous in the latitude-longitude-time domain. Since these criteria are similar to those used in this study, Dias et al. (2012) provides a valuable subject of comparison with respect to discussing differences in lifespan, system width, and propagation speed. Like Wheeler and Kiladis (1999), Dias et al. (2012) is a study on tropical waves and an attempt to tease out specific equatorial wave types from an observational record, albeit from a different data source.

The study most similar to this one is Skok et al. (2009), as it uses calculated rain rates directly for the purposes of system identification. Skok et al. (2009) takes a method for identifying precipitating systems originally developed for verifying weather forecasts and applies it to two satellite-derived rainfall products to track precipitating "objects" in the Pacific Ocean from 39°N-39°S. The two rainfall products used are the TRMM 3B42 Multisatellite Precipitation Analysis (TMPA; Huffman et al. 2007) product, which is a merged microwave and geostationary infrared product, and a product that uses an adaptive neural network calibration of geostationary infrared to TMI called Precipitation Estimate from Remotely Sensed Information using Artificial Neural Networks (PERSIANN; Hsu et al. 1997). Both products are 0.25°x0.25° resolution and are used for 3-hourly rainfall accumulation, the same spatial and temporal resolution as the CMORPH product used to track systems in this study. Skok et al. (2009) also arrived at using the same

7mm/hr rain rate threshold of defining a system as used in this study, making it ideal for comparisons that will be given in Section 4.

A few recent studies have examined the precipitation characteristics of cloud regimes as defined by ISCCP in Rossow et al. (2005). Jakob and Schumacher (2008) use TRMM PR overpasses to analyze the precipitation and latent heating characteristics of ISCCP cloud regimes in the Tropical Western Pacific, finding three precipitation regimes with distinct characteristics and daily rain rates. Lee et al. (2013) uses the same ISCCP cloud regime data from a 10-year period and 35°N-35°S. That study also uses a gridded rainfall product, TMPA, to examine the rain rate tendencies for each cloud regime, finding that the deep convective cloud regime (WS1) accounts for the largest rain rates and the majority of total rainfall accumulation in the Tropics. WS1 is also found to be rain-free approximately half the time. Lastly, Rossow et al. (in review) also uses the ISCCP cloud regime scheme, specifically examining extreme Tropical precipitation, which is defined as rain rates greater than 2mm/hr. The authors find that extreme rainfall exists in 40% of WS1 occurrences, with other convective cloud states accounting for a much smaller fraction of extreme precipitation. Some of the main findings from Lee et al. (2013) and Rossow et al. (in review) are corroborated later in this study.

1.5 Overview

The aforementioned data products, CMORPH and GProf data from TMI, are used to categorize and track deep convective MCSs in the tropical oceans. This method is then combined with state variable data from various sources and data on cloud type to provide a full picture of the mean effect a deep convective MCS has on its environment. This analysis alone sheds light on processes that affect the water and energy cycle on local to regional scales; however, since both sets of data rely on passive microwave observations, it is also worth discussing possible biases in this type of observation and how these issues can relate back to the larger problem of closing the observational energy budget of the Earth.

Deep convective raining systems can have a sizable impact on local energy budgets. The passage of an MCS can alter many key meteorological state variables, both temporarily and by way of a net impact. For example, deep clouds limit the radiative heating of the surface, gusting winds that result from downdrafts enhance oceanic evaporation, cool rain causes sea surface temperature to dip slightly, and the total amount of water vapor in the atmospheric column is depleted by the storm's passage, possibly decreasing the likelihood a similar system passing through in the near future. These types of local impacts aren't well understood in a mean sense, and are indeed a focal point of this study. In a changing climate, a shift in the frequency of certain types of storms could have climate impacts at the regional scale, proving it useful to understand the mean behavior of these systems in order to verify that climate models accurately reproduce the effects witnessed in nature.

Vertical structure of the atmosphere, including the presence of different cloud types, is of crucial importance to the precipitation characteristics of a given scene. Very generally, the precipitation characteristics of a system can be inferred by looking at the temperature and height of cloud tops, since these traits imply the cloud type and the microphysical state of the precipitation (e.g. Lau and Wu 2011; Elsaesser et al. 2010; Johnson et al. 1999). The state of the atmosphere, as described by the myriad variables that comprise elements of the water and energy cycles, is what ultimately defines cloud type and the distribution of cloud types in a given region. For instance, there tend to exist more convective, deep, ice-phase clouds in the Pacific warm pool than in the southeast Pacific near Peru due to one environment favoring deep cloud development and the other suppressing it. This is due to differences in latitude, mean vertical movement in the atmosphere, moisture convergence, and other factors driven by the general atmospheric circulation.

Retrieval algorithms determine the vertical structure of the atmosphere often by combining physically observed parameters with information from databases and cloud resolving models. For the same SST and TPW, the algorithms run the same retrieval for a pixel near Peru as a pixel near New Guinea, and should arrive at the same rain rate if the input is exactly the same. Since retrievals do not account for many unknown quantities such as aerosol content, assumptions are made that are inevitably the same in one part of the world as those made somewhere else. Certain regional biases can then emerge in rainfall data products; many studies examine such regional biases and attempt to ascribe these retrieval biases to factors such as aerosol optical depth or total precipitable water (Berg et al. 2006). Small variations in certain variables that affect the vertical structure of the atmosphere can have significant effects upon microwave retrievals, as shown in studies that examine retrieval biases; these small variations in the environment as a function of region are a focus of this study.

The way forward, then, is to deepen our understanding of precipitating systems in a mean sense, yielding knowledge that can be translated into better retrievals and more accurate models. This study does not pretend to answer any of the large problems previously stated regarding the global energy cycle; it aims to shed some light on a few key elements of the water and energy cycle, broadening the base of knowledge that will eventually fill in some of these gaps.

2. DATA SETS

2.1 TMI and GProf

The Tropical Rainfall Measuring Mission (TRMM) satellite carries two instruments used in this study, the TRMM Microwave Imager (TMI) and Precipitation Radar (PR). It orbits the globe at a rate of approximately 16 orbits per day, covering the Earth from 38°N-38°S. The TRMM satellite was in a 350km circular orbit from its launch in 1997 until it was boosted to a 402km orbit in August 2001 to save fuel. All of the data used in this study are taken from after the boost to prevent introducing any unneeded biases. The TMI instrument is a dual-polarized, nine-channel passive microwave radiometer with a total swath width of 878km, with 208 pixels per scan and around 2920 scans per orbit. The antenna of TMI rotates at 31.6 revolutions per minute at a view angle of 52.8° to the surface.

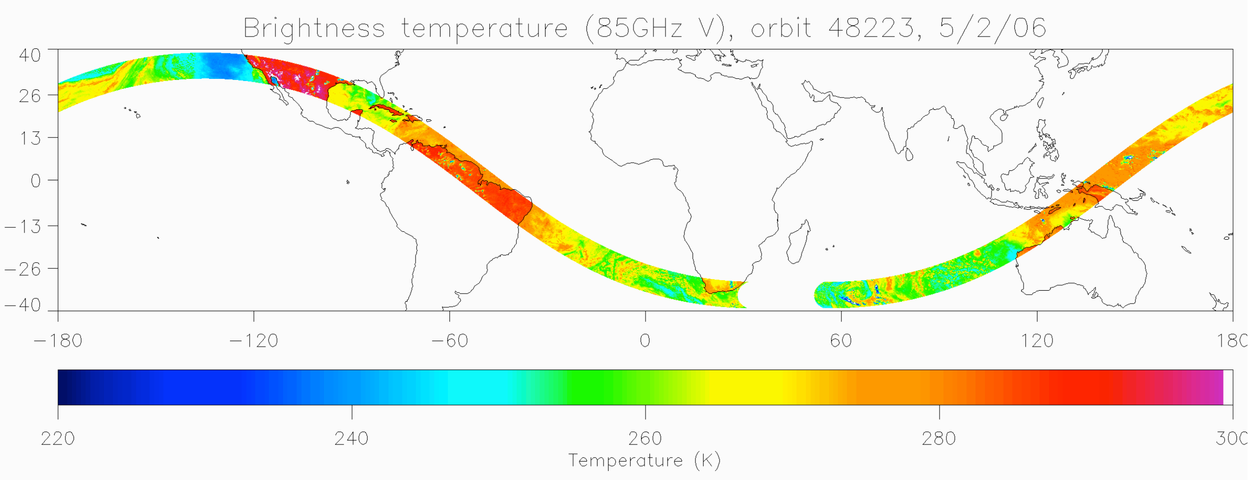

Figure 2.1. Brightness temperatures from one orbit of TMI on the 85.5GHz vertically polarized channel.

The Goddard Profiling algorithm (GProf) is a microwave retrieval developed originally for use with the various SSM/I instruments and the then upcoming TMI instrument (Kummerow et al. 1996). Many refinements over the years (e.g. Kummerow et al. 2001;

Kummerow et al. 2011) have led to the latest version of the algorithm, version 2010. This version of GProf is currently used as the operational rainfall retrieval algorithm for both the TMI and AMSR-E instruments.

GProf uses a pixel size that is fitted to the 19.35GHz channels, which have an instantaneous field of view of approximately 30km x 18km. A detailed description of all the technical aspects of the TMI instrument is available in Kummerow et al. (1998). For each pixel a Bayesian retrieval is performed in which observed T_bs, knowledge from observationally-generated databases, and previously calculated probability density functions are combined to determine the value for each variable being calculated. An improvement from GProf version 2004 to version 2010 is that the a priori database used, which was dependent on cloud resolving models and had issues due to representativeness errors (Kummerow et al. 2006), is now determined by observed TRMM radar and radiometer measurements (Kummerow et al. 2011). The three variables calculated in the GProf retrieval that are used in this study are rainwater path (RWP), surface rain rate, and convective/stratiform rain rate.

2.2 Precipitation Radar

The TRMM Precipitation Radar (PR) is the first ever space-borne radar instrument. The TRMM PR has a 247km swath width (post-boost), essentially having the same view as the middle 28% of the TMI swath. Some data from the PR 2A25 product is used in this study to demonstrate self-similarity among the clusters defined by data from TMI GProf output. The PR instrument, despite being space-borne, functions in the same way as most radars in that it yields reflectivity values that are then used to calculate rain rates based upon certain assumed drop size distributions. A path integrated attenuation value is also calculated to aid in determining the rain rate. The 2A25 product provides rain rates and reflectivity values for 80 vertical levels from the surface to 20km in altitude, each measuring 250m in depth. In each scan there are 49 angle bins, or pixels. Again, further technical information on the TRMM PR instrument and its geometry is available in Kummerow et al. (1998).

2.3 Cloud regimes

Data from the International Satellite Cloud Climatology Project (ISCCP) are used to show agreement between the system categorization method used in this study and an independent dataset of a different but highly related atmospheric field, and also to examine the evolution of cloud fields before and after the passage of a heavily raining MCS. The data used are the pre-determined cloud clusters, or "weather states," from Rossow et al. (2005). This pre-clustered dataset is freely available from the ISCCP website. The weather state data span the entire Tropics from 15°N-15°S at a 2.5° grid resolution at 3-hourly intervals, the same resolution as the ISCCP D1 dataset from which it is derived (Rossow and Schiffer 1999). This dataset is available from July 1983 to December 2004.

The ISCCP cloud clustering method utilizes visible satellite imagery as well as infrared observations, so it is useful only during time periods in which the sun is shining on each grid box. The clustering algorithm that created the dataset used histogram distribution data of cloud top pressure and cloud optical thickness to determine the six dominant weather states (shown in Figure 2.2). An example of the gridded cloud regime dataset is shown in the top panel of Figure 2.3, with GProf-derived RWP from TMI from the same date for the sake of comparison. The gray pixels signal areas in which there was insufficient solar radiation incident upon the Earth's surface, and thus no data.

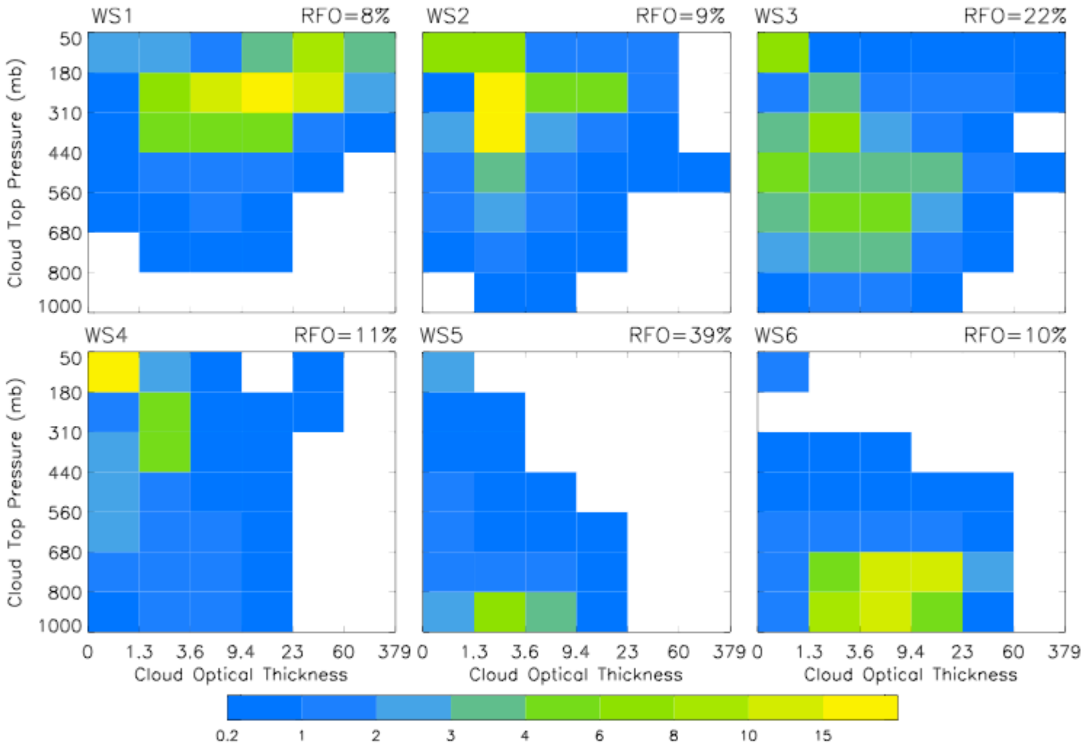

Figure 2.2. ISCCP weather state distributions of cloud top pressure and optical thickness, given with frequencies of occurrence for each regime in the Tropics. From Rossow et al. (2005).

The six cloud (weather state) classifications, as defined in Rossow et al (2005), are given in Table 2.1. WS1 marks the most vigorous deep convective mesoscale weather state and is the state into which most systems tracked into this study fall. The regimes of WS1-3 are the convectively active states, with WS4-WS6 being labeled convectively inactive. Since only two years of the ISCCP D1 data record match up with the period used in this study, ISCCP data is used only from 2003 and 2004.

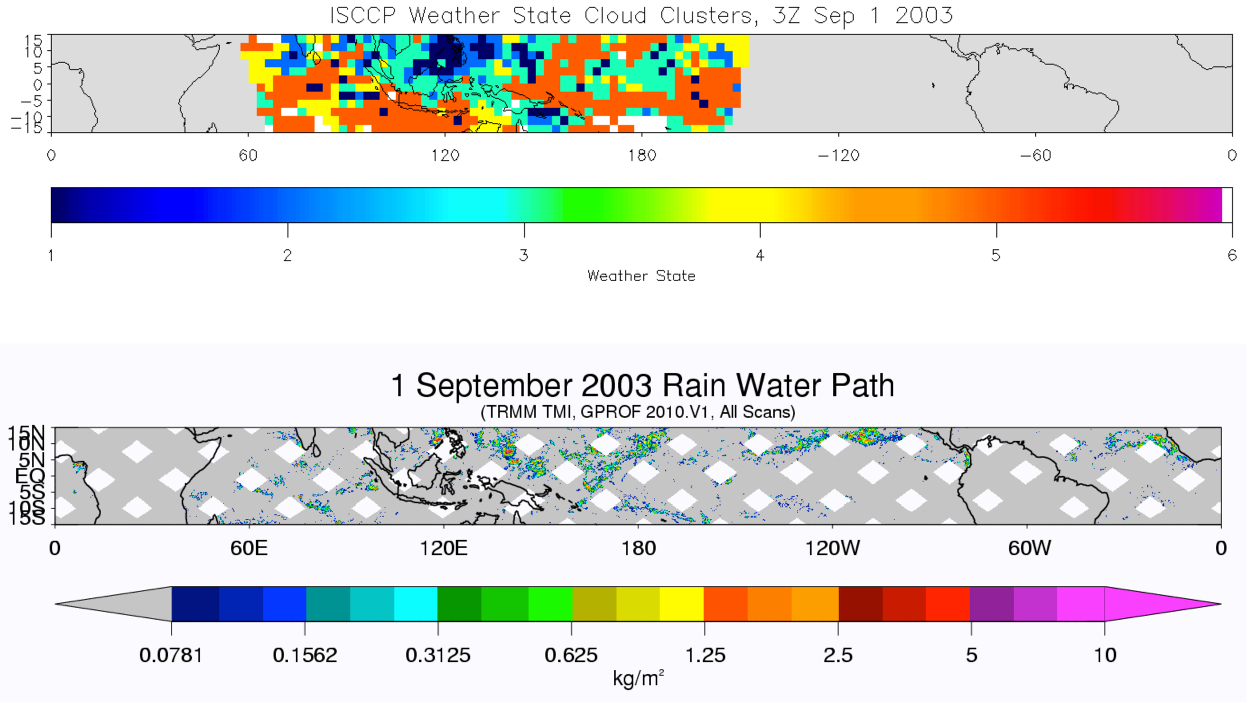

Figure 2.3. The top panel shows ISCCP weather state data from one time step, with missing data in black and darkness in grey. The bottom panel shows GProf-derived RWP from the same day for comparison, courtesy http://rain.atmos.colostate.edu/RAINMAP10/.

Table 2.1. ISCCP weather states frequencies of occurrence, for the Tropics and Tropical Ocean.

Cloud Regime	Description	Frequency	Frequency (ocean)
WS1	Vigorous deep convection	8%	8%
WS2	Thick cirrus, less vigorous convection	9%	9%
WS3	Isolated, smaller-scale convection	22%	21%
WS4	Thin cirrus	11%	11%
WS5	Scattered cumulus	39%	39%
WS6	Marine stratus	10%	12%

2.4 State variables

To analyze the mean effect an MCS has on its local environment, state variables are culled from a few sources that provide data on 3- or 6-hourly, high spatial resolution grids. Sea surface temperature (SST) and surface latent heat flux (LHF) data are taken from the SeaFlux dataset (Clayson et al. (in preparation)). Information regarding water vapor and wind fields is taken from the European Center for Medium-range Weather Forecasting Interim Reanalysis product (Dee et al. 2011). Lastly, information regarding longwave radiation, and shortwave radiation as well as cloud fraction, comes from the Surface Radiation Budget (SRB) 3.1 release and 3.0 release products, respectively (Stackhouse et al. 2011). All datasets mentioned are used to provide high-resolution data on the state of the atmosphere for the years of 2003 through 2007.

2.4.1 SeaFlux

The SST and LHF data used from SeaFlux comes on a ¼ degree global grid. Both SST and LHF from SeaFlux are used in this study at 3-hour intervals, in spite of SeaFlux SST being available as an hourly measurement. These data products are based wholly upon satellite data, with the satellite data blended together before being gridded. The SST measurements use the same basic method as the widely vetted Reynolds SST dataset (Reynolds et al. 2007), but then apply a diurnal parameterization to calculate the hourly SST values (Bogdanoff and Clayson (in preparation)). The LHF data is calculated using satellite-derived values for wind speed, air-sea humidity difference, and sea surface roughness. LHF is given in Watts per square meter, and is proportional to the surface's rate of evaporation. SeaFlux data are available from 1998 through 2007.

2.4.2 ECMWF Interim Reanalysis

The ECMWF Interim Reanalysis (Dee et al. (2011); hereafter ERA-Interim) is a reanalysis product that uses 4d-Var assimilation techniques to blend millions of observations from myriad sources to produce a full picture of the global atmosphere. Three fields from ERA-Interim are used in this study to calculate water vapor at various atmospheric levels and to calculate the net divergence of precipitable water out of the atmospheric column. This is accomplished using two wind fields (zonal and meridional wind vectors) and specific humidity data at 37 pressure levels from 1000 to 1hPa. The ERA-Interim data is on a 1.5° global grid at a 6-hourly time resolution. Water vapor is calculated at each pressure level by finding the mean specific humidity of the layer, multiplying by the change in pressure from the bottom of the layer to the top, and dividing by the acceleration due to gravity (*g*), yielding a water vapor value for each layer in units of kg/m^2.

$$\frac{1}{g} * q[z] * \Delta P[z] = wv[z]$$

Once the layer values are calculated, total precipitable water (TPW) is simply the sum total of all layer values. The divergence of water vapor out of the atmospheric column is a more complicated calculation. The divergence of water vapor is determined for each layer in the atmospheric column as shown below. To determine columnar divergence, there is a sum over all layers. A factor of 3600 is needed to change the final units from a flux of kilograms of water per second per square meter into millimeters per hour, a common unit for precipitation and evaporation rates. This conversion is possible due to the density of water, from which it follows that 1mm of water per square meter is equal to 1kg/m^2. The net fluxes are divided by twice the width of the box in that dimension to cancel the unit of distance from the wind velocity term. Zonal distance (notated *londist*) is a function of latitude while meridional distance (*latdist*) is constant regardless of longitude. Because the divergence operator is acting on a product, the chain rule must be used, as seen below. The column divergence of a given grid box is thus given by the sum total net flux of water vapor through the two meridional boundaries of the box plus the total net flux of water vapor through the two zonal boundaries, multiplied by the pressure difference and divided by gravity.

$$\nabla \bullet vq[x,y,z,t] = \frac{1}{g}\left\{ \begin{array}{l} \dfrac{q[x,y,z,t]*(u[x+1,y,z,t]-u[x-1,y,z,t])+u[x,y,z,t]*(q[x+1,y,z,t]-q[x-1,y,z,t])}{2*londist[y]}+ \\ \dfrac{q[x,y,z,t]*(v[x,y+1,z,t]-v[x,y-1,z,t])+v[x,y,z,t]*(q[x,y+1,z,t]-q[x,y-1,z,t])}{2*latdist} \end{array} \right\} *\Delta P[z]$$

$$\nabla \bullet Q[x,y,t] = \sum_{z=0}^{TOA} \nabla \bullet vq[x,y,z,t]*3600$$

Using the methods shown above, values are calculated for the variables of total precipitable water in the atmospheric column (TPW), the convergence of water vapor into the atmospheric column ($-\nabla \bullet Q$), and total water vapor in three levels of the atmospheric column, namely from the surface to 850mb, 850mb to 500mb, and 500mb to the top of the atmosphere. Data from ERA-Interim are available from 1979 through 2012. Figure 2.4 below shows how well water vapor and precipitation estimates from ERA-Interim compare to independently calculated observational products from GPCP and Remote Sensing Systems (RSS).

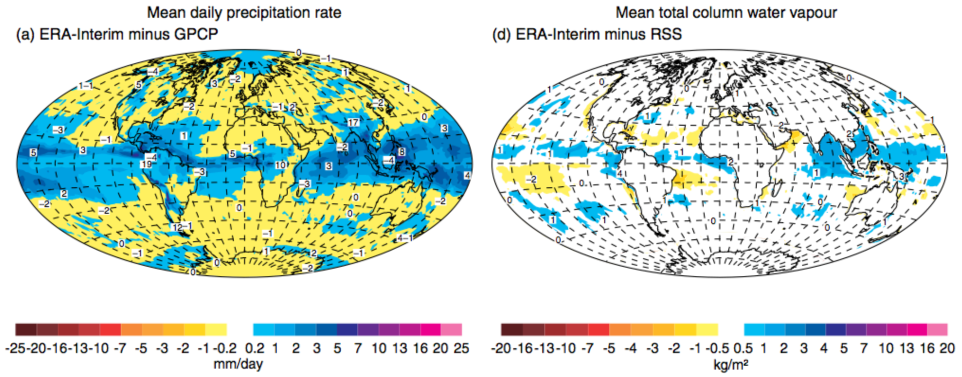
Mean daily precipitation rate
(a) ERA-Interim minus GPCP

Mean total column water vapour
(d) ERA-Interim minus RSS

Figure 2.4. ERA-Interim precipitation compared to GPCP (a), and total column water vapor compared to a product from RSS (d). From Dee et al. (2011).

The wind vector fields from ERA-Interim are also used to calculate vertical wind shear magnitude. These are the same wind vectors at 37 pressure levels used to compute water vapor divergence. Wind shear magnitude is calculated at each pressure level using the following formula:

$$shear[x,y,z,t] = \frac{\sqrt{(U[x,y,z+lev,t]-U[x,y,z-lev,t])^2+(V[x,y,z+lev,t]-V[x,y,z-lev,t])^2}}{\sum deltaZ[z-lev:z+lev]},$$

where U and V are the wind vectors at each pressure level in meters per second and deltaZ is the change in altitude from one pressure level to the next in meters. Shear can be calculated between two layers, four layers, or more by adjusting the variable *lev*.

2.4.3 Surface Radiation Budget

Radiation data come from the Surface Radiation Budget (SRB) dataset, releases 3.0 and 3.1 (Stackhouse et al., 2011). Both longwave and shortwave data products come at a 3-hourly time resolution on a 1° global grid. Net longwave radiation at the surface is calculated at each grid point by subtracting upward longwave from downward longwave radiative flux; net shortwave radiation at the surface is similarly calculated, by subtracting upward shortwave from downward shortwave radiative flux. Total net flux into the surface is simply net shortwave flux plus net longwave flux. In addition to offering net surface radiative fluxes, the SRB dataset provides a measurement of cloud fraction that is also used in this study. Comparisons between the SRB dataset and other surface flux datasets found a general flux component agreement in global averages to about 5-10 W/m^2 (Stackhouse et al. 2011). SRB radiative estimates have been found to be significantly more consistent with other observations over ocean, as orography and aerosol content don't affect the accompanying ancillary data as much as over land. SRB data are available from 1983 through 2007. As an example, below is one 3-hour time step of SRB net radiative flux at the surface, showing the expected maximum of net surface heating at the International Date Line at 0Z.

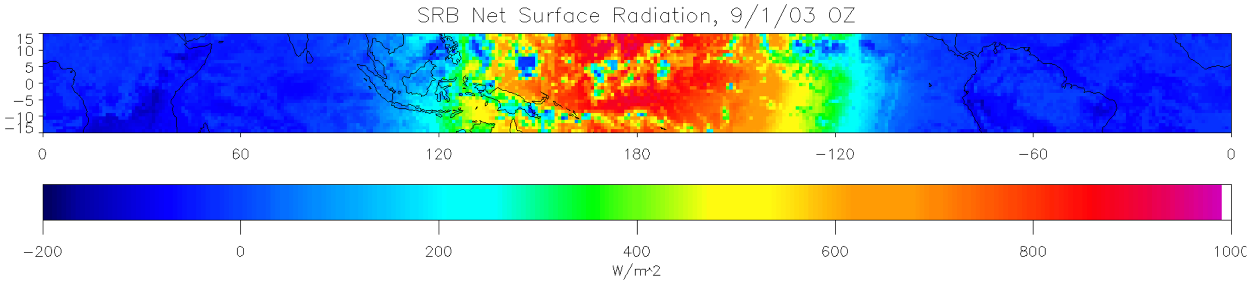

Figure 2.5. Net surface radiation derived from SRB data. Compare to Fig 2.3.

2.4.4 Global Tropical Moored Buoy Array

In-situ measurements of SST from buoy data are taken from the Global Tropical Moored Buoy Array (McPhaden et al. 2010). The GTMBA is a constellation of moored buoys comprised of the Tropical Atmosphere Ocean/Triangle Trans-Ocean Buoy Network (TAO/TRITON) in the Pacific Ocean, the Prediction and Research Moored Array in the Tropical Atlantic (PIRATA), and the Research Moored Array for African-Asian-Australian Monsoon Analysis and Prediction (RAMA) in the Indian Ocean. The buoys used in this study provide high-resolution data at either hourly or 10-minute intervals. SST measurements from the buoys are given as the ocean temperature at a depth of 1m, with a few buoys using a depth of 1.5m, an important distinction from ocean skin temperature, which varies much more on short timescales due to diurnal heating (Kawai and Wada 2007). Only measurements that were given one of the two highest quality codes (“highest quality” and “default quality”) are used in this study. The absolute accuracy of the buoy SST measurements is ±0.003°C (Freitag et al. 1999).

3. METHODS

3.1 Tracking

An algorithm was developed which tracks groups of contiguous CMORPH pixels that exceed a defined rain rate threshold. The region chosen for analysis is the Tropical Ocean between 15°N and 15°S. By contiguous it is meant that the pixels exceeding the threshold are adjacent along at least one lateral edge in the same time step or one time step removed (Figure 3.1). The algorithm groups the contiguous pixels and assigns each group a number, permitting each group to be followed as it moves in space and time. Additionally, a group must contain a minimum amount of total pixels across all time steps to be considered. This removes small, anomalous areas of high rain rates and very short-lived systems from the analysis. A mean latitude and longitude of each group is calculated at every time step so as to allow co-location with other datasets. CMORPH data is of a high enough resolution in time and space to resolve most mesoscale convective systems.

Choosing the rain rate threshold for tracking is important for keeping distinct systems separate. A low threshold causes there to be too many pixels that overlap and thus systems that are artificially large and propagate very long and far. A high threshold will cause some systems to be missed and some systems with less cohesive areas of high rainfall to be incorrectly labeled as separate mesoscale entities. The rain rate threshold that was chosen, separating pixels that are eligible to form tracked groups from non-eligible pixels, is a rain rate of 7mm/hr. This threshold is the same as the mean scene rain rate found in the deep convective regime derived from TMI. Determination of the rain rate threshold for tracking was made after performing a sensitivity analysis, examining thresholds between 5 and 10 mm/hr. The threshold of 7mm/hr maximized the number of eligible groups, as higher thresholds missed some distinct systems while lower rates caused clumping of some distinct groups together into large amorphous blobs of rain. Visual inspection was important in verifying that the threshold was indeed reasonable.

An overall view of tracked system characteristics is found in Figure 3.2, incorporating every system meeting the stated criteria for 2003 through 2009, with results separated by ocean basin. The criteria are that systems exist between 15°N-15°S, contain contiguous CMORPH pixels of >7mm/hr, and exist for at least 6 hours with a minimum of 40 total (quarter degree) pixels. This last requirement helps to ensure that systems occupy an area sufficient to allow comparison with this study's own categorization scheme (Section 3.2) as well as with other studies (Elsaesser et al. 2010; Masunaga 2012); changing it does not significantly alter the results seen in Figure 3.2 apart from causing there to be more short-lived systems. The ocean basins are defined by the longitude at which a system ends (Table 3.1). Some key conclusions from this analysis are that westward-propagating systems are more common and generally faster moving (a topic explored in Tulich and Kiladis 2012), not many systems have lifetimes in excess of 24 hours, and that the ocean basins possess strikingly similar distributions of behavior. The Atlantic basin is a slight outlier in that it contains the largest ratio of west- to east-propagating systems, and has west-movers that tend to travel greater distances due to a tendency for many Atlantic systems to move quickly westward.

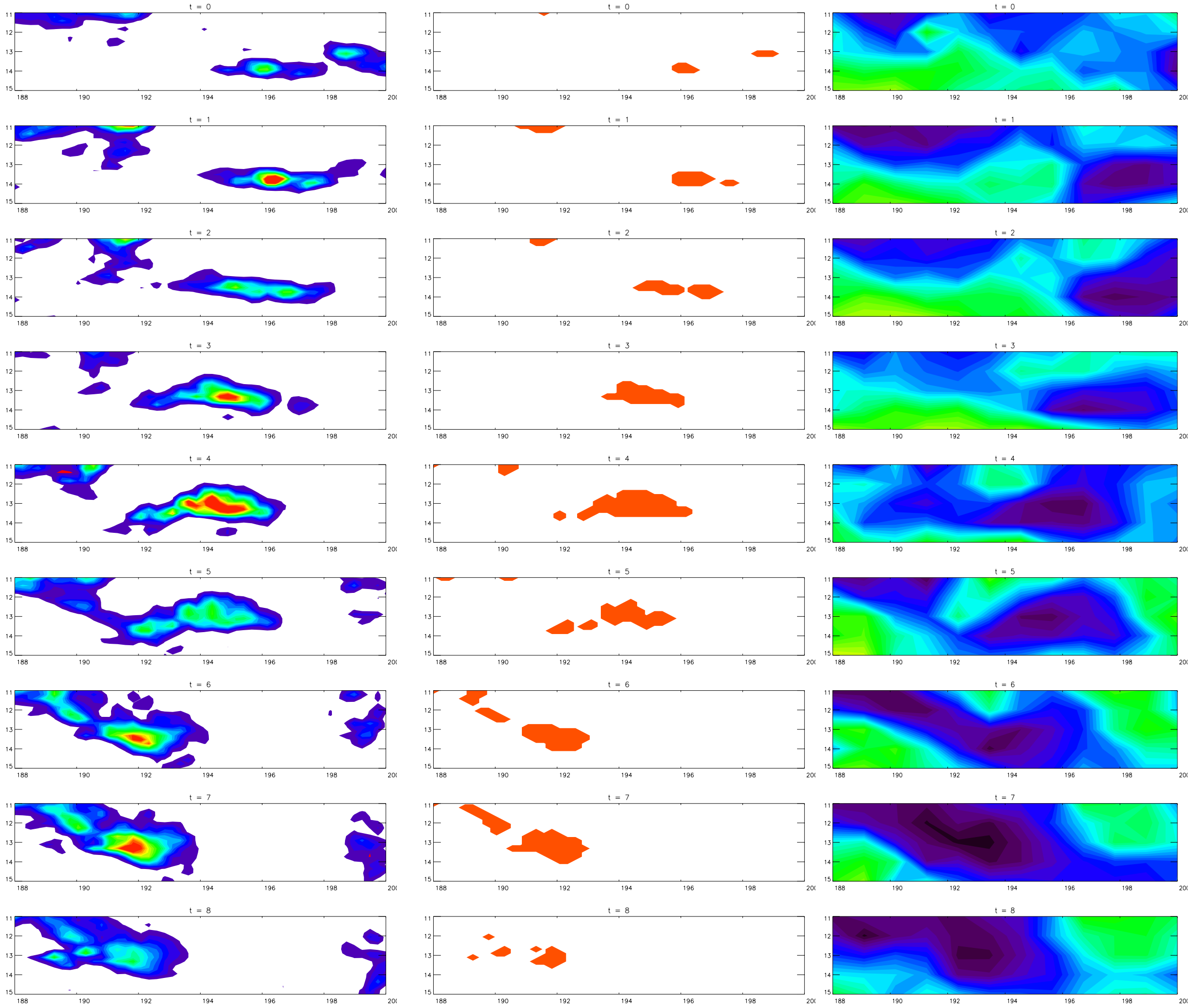

Figure 3.1. A sample tracked system. Pixels that meet the rain rate threshold (center), all rain rates above 1mm/hr (left), and outgoing longwave radiation (right) for comparison.

A main finding of this study is that the biggest determinant of a MCS's impact on the environment is its speed of propagation. To aid in separating out these impacts, all following analysis is separated into fast- and slow-moving systems. Fast systems are defined to have a mean propagation speed greater than 6m/s while slow systems propagate at less than 2m/s; these limits were chosen for their simplicity and the similar number of systems that fall within those bounds.

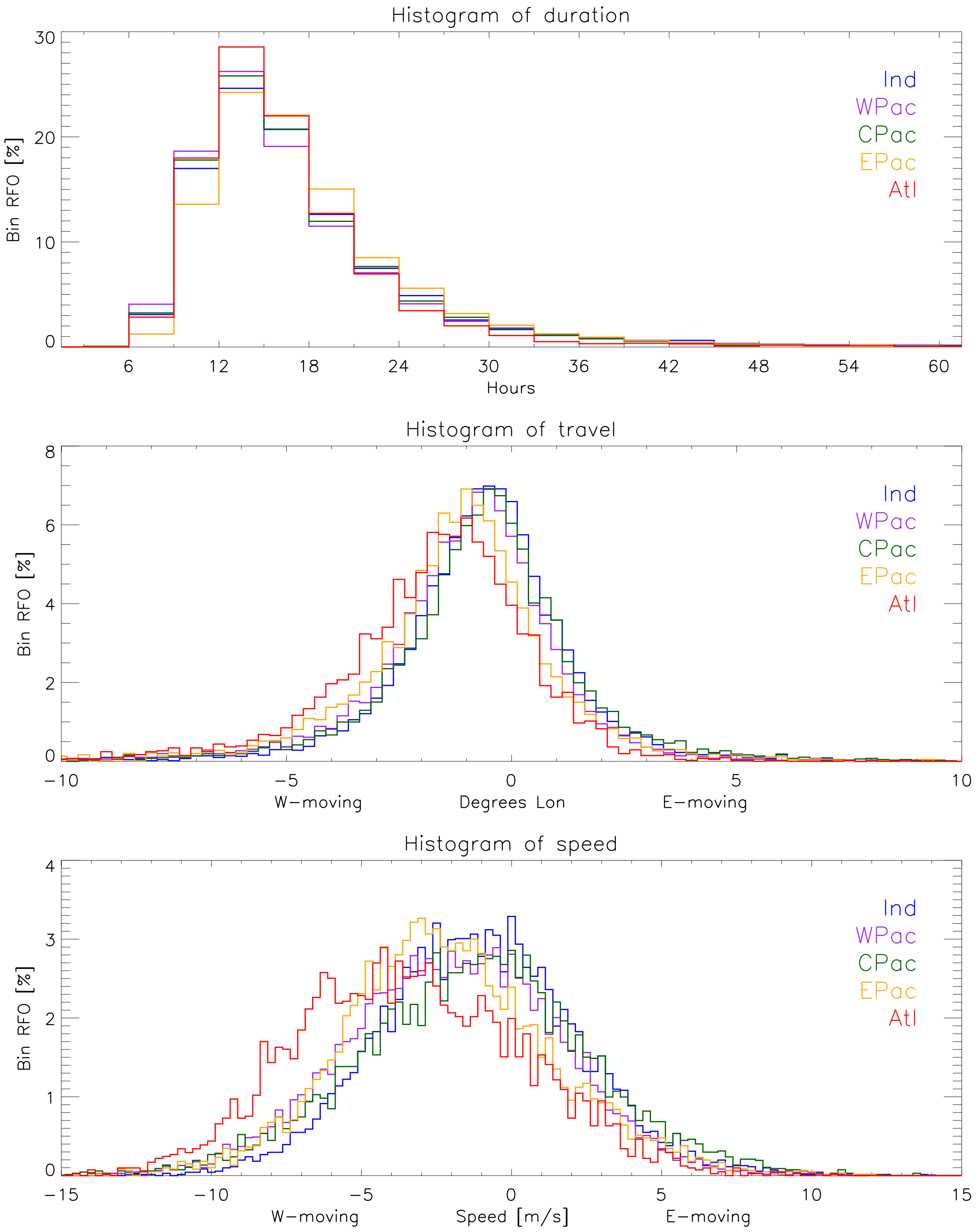

Figure 3.2. Histograms of all tracked systems from 2003 through 2009, separated by basin.

Table 3.1. Means and standard deviations of latitude [°N], propagation speed [m/s], and number of quarter degree pixels per time step for all tracked systems 2003-2006, shown for fast and slow systems in all five ocean basins.

		Indian (30-100°E)	West Pacific (100-170°E)	Central Pacific (170-220°E)	East Pacific (220-300°E)	Atlantic (300°E-30°W)
Latitude	Fast	-1.1 ± 7.3	1.9 ± 6.9	0.4 ± 8.4	8.0 ± 3.4	5.0 ± 4.4
	Slow	-3.6 ± 7.8	-0.2 ± 8.9	-0.6 ± 9.0	7.6 ± 4.8	4.5 ± 5.2
Speed	Fast	7.4 ± 1.4	7.8 ± 1.6	8.1 ± 1.9	7.8 ± 1.7	8.0 ± 1.6
	Slow	1.3 ± 0.4	1.3 ± 0.5	1.3 ± 0.5	1.3 ± 0.5	1.3 ± 0.4
Size	Fast	11 ± 9	12 ± 11	12 ± 11	11 ± 9	11 ± 9
	Slow	26 ± 17	24 ± 18	31 ± 24	29 ± 21	26 ± 20
Cases	Fast	2562	6204	4340	3731	3843
	Slow	5296	6696	4926	4164	1628

Table 3.2. Fraction of time steps within local solar time (LST) bins for all tracked systems 2003-2006, shown for fast and slow systems in each ocean basin.

		0-3	3-6	6-9	9-12	12-15	15-18	18-21	21-24
Ind	Fast	0.14	0.15	0.15	0.12	0.11	0.10	0.11	0.12
	Slow	0.14	0.14	0.14	0.13	0.12	0.11	0.11	0.12
WPac	Fast	0.14	0.16	0.15	0.13	0.10	0.09	0.10	0.12
	Slow	0.14	0.15	0.15	0.13	0.11	0.10	0.10	0.11
CPac	Fast	0.14	0.15	0.14	0.13	0.11	0.10	0.11	0.12
	Slow	0.14	0.15	0.15	0.13	0.11	0.10	0.10	0.12
EPac	Fast	0.13	0.15	0.14	0.13	0.12	0.10	0.10	0.12
	Slow	0.14	0.16	0.15	0.14	0.11	0.09	0.09	0.12
Atl	Fast	0.13	0.15	0.15	0.14	0.12	0.10	0.10	0.12
	Slow	0.13	0.16	0.16	0.14	0.11	0.09	0.09	0.12

As seen in Figure 3.2, the tracked systems' duration peaks at 12-15hrs and there are significantly more systems that move to the west. Dias et al. (2012) provides a good subject of comparison for these results, as it uses the same latitudinal domain. Despite tracking "continuous cloud regions" instead of precipitation rates, the ratio of west- to east-moving systems is consistent with this study, as is the finding that westward propagating systems have faster speeds on average. Skok et al. (2009) also found a predominance of westward-propagating systems in the Tropical Pacific. Dias et al. (2012) finds a peak in the duration of propagating cloud regions of 18-24hrs. This discrepancy with the results presented here can be due to the finer grid used in this study, which can identify smaller-scale systems, as well as this study's focus on heavy precipitation instead of only cold cloud tops. Deep clouds with cold cloud tops persist much longer than strong precipitation does, a result shown in Section 4.2.

3.2 Categorization

3.2.1 Motivation and background

Analysis of a specific type of tropical precipitating system, namely heavily precipitating systems with large-scale deep convection, necessitates a method by which one can discriminate between many systems with diverse characteristics. For this to be successful, the method for separating systems into various regimes has to be objective and statistically grounded. The implementation of such a method can then provide a valuable framework in which different rainfall regimes are examined, assuming that each regime possesses sufficient self-similarity to be significantly different from the other regimes.

The inspiration behind the clustering method used in this study is work done in Elsaesser et al. (2010), in which a K-means clustering method applied to precipitating scenes in the Tropical Ocean found three distinct, self-similar classes. That study uses two years of data from TRMM PR, grouping square, oceanic patches of approximately 1°x1° surface area into clusters interpreted as deep, mid-level, and shallow convection fields. The mid-level regime contains elements of both the shallow and deep convective regimes while lacking mesoscale organization, suggesting either an in-between state in the convective lifecycle or a state with convection not strong enough to produce large-scale deep clouds. Self-similarity of the regimes is shown largely through latent heating profiles.

A possible drawback of using a K-means clustering method is that the algorithm will yield whatever number of clusters it is prompted to return. For instance, if given a Poisson distribution with no pattern to it whatsoever, the algorithm will inevitably find two clusters or eight clusters if the input given is two or eight, despite the complete lack of a physical basis for the returned grouping. Similarly, if the input data are grouped clearly into two distinct regions of n-dimensional space and the algorithm is prompted to find four clusters, it will likely split the two distinct regions into subsets of each that are probably not distinct. It is here that the idea of self-similarity is crucial, in that the algorithm's output needs to be judged for whether or not it carries real physical meaning. In Elsaesser et al. (2010), the three precipitation regimes exhibit very consistent properties within each cluster, such as heating profiles and rainfall characteristics, regardless of when or where they occur. The three clusters are found to be consistent as well as physically reasonable, given the literature on the 'building blocks' of the convective lifecycle (Mapes et al. 2006) and the trimodal characteristics of tropical clouds (Johnson et al. 1999). It is the goal of this section to explain how the precipitation regimes in this study are derived and why they are physically meaningful.

3.2.2 Technical aspects

The K-means clustering algorithm (Anderberg 1973) is a method for grouping elements of a dataset to elucidate connections, given any number of variables. It is a method used by numerous recent studies on clouds and precipitation (e.g. Rossow et al. 2005; Jakob and Tselioudis 2003; Elsaesser et al. 2010). The algorithm iteratively searches for a predefined number (k) of clusters given n independent variables that define each data point. The iterative process starts with *k* elements of the *N* total elements in *n*-dimensional space, essentially *k* clusters of one element each, to function as seed points (centroids). The remaining (*N*-*k*) elements are given the cluster label of the centroid closest to it in Euclidean distance in the *n*-dimensional space. After each new data point is given a cluster assignment, the centroid of the cluster is recalculated. Once all elements have been assigned to a cluster, the final centroids are used as new seed points when the algorithm is iterated. Depending upon the actual grouping of the data and the number of iterations performed, the algorithm should converge to *k* centroids that do not change with further iteration.

Before the clustering algorithm is applied, a month of TMI data is processed by the GPROF retrieval to obtain the desired variables of rainwater path, surface rain rate, and convective rain rate. Roughly following the example of Elsaesser et al., the orbit data are divided into 'scenes' that are roughly 100km boxes, approximating the area of a 1°x1° grid box in the Tropics (a similar scene size is also used in Masunaga 2012). This is done by splitting up the total width of the TMI scan into six separate but adjacent scenes. Each scene is 29 pixels by 9 scans, in the parlance of TMI's geometry, causing there to be approximately 1900 scenes per orbit, yielding around 700,000 possible scenes per month. A scene only qualifies as being 'precipitating' if it contains at least one pixel with a rain rate greater than 0.5mm/hr, a cutoff similar to the minimum rate detectable by TRMM PR. Also, to keep the scene size from changing too much with latitude, only scenes within the bounds of 30°N-30°S are considered. Scenes containing any pixels that aren't 100% ocean are also discarded. Each month produces around 140,000 valid scenes that are fed into the clustering algorithm.

Five variables are used as input for the clustering algorithm. Each of these variables represents the state of the entire scene, not just the precipitating pixels. Two of the variables are simply means of the scene, namely convective rain rate and the fraction of rainfall that is convective. Convective rain rate is an output parameter in the retrieval algorithm, whereas the convective fraction of rainfall is calculated externally by dividing the total convective rainfall by the total surface rainfall of the scene. These two variables provide information on the scene's overall rain rate as well as how much rain is stratiform and convective, an attribute that is highly related to distinct cloud states (Jakob and Schumacher 2008). The other input variables come from a normalized histogram of rainwater path (RWP). Split up into three bins (less than 0.3kg/m^2, 0.3-1.8kg/m^2, and greater than 1.8kg/m^2), the histogram of RWP provides a sense of the distribution of cloud depths in each scene, since RWP scales closely with optical depth. The input variables chosen supply data valuable to a determination of the state of a scene, together providing information on both precipitation and cloud state. All the input variables are standardized before going into the clustering algorithm to ensure that each variable is given equal weight.

The method presented here, executed with a cluster number (*k*) of 3, yields a very stable set of clusters whose centroids vary very little from month to month. An average month has a distribution of scenes such as 82% shallow, 17% mid-level, and 1% deep convective. The shallow, mid-level, and deep clusters exhibit mean scene rain rates of approximately 0.18, 1.6, and 7mm/hr, respectively, with these regimes accounting for 36%, 48%, and 16% of total oceanic rainfall accumulation from 30°N-30°S. Nearly two-thirds of all rainfall comes from a mere 18% of scenes, underscoring the importance of heavily raining systems in the overall water and energy budgets.

It is important to stress that ascribing the relative importance of different precipitation regimes depends greatly upon how those regimes are defined. For comparison, a method of defining Tropical rainfall regimes that uses cloud area and brightness temperatures from 85GHz radiometer measurements (Mohr et al. 1999), determined that mesoscale convective systems account for 70-80% of all Tropical precipitation. Despite different definitions and nomenclature, that study's conclusions match with others (e.g. Lee et al. (2013)), in that large-scale deep convection accounts for a majority of Tropical rainfall. The exact values of something like the percentage contribution to total rainfall will vary, but conclusions hold between studies that employ very different methods. The categorization method employed in this study is in accord with those broad conclusions.

3.2.3 Statistical foundation

Arriving at a statistically rigorous justification for the number of clusters chosen is not straightforward. In studies that use the K-means algorithm to find similar weather characteristics (Rossow et al. 2005; Jakob and Tselioudis, 2003; Elsaesser et al. 2010), each one uses a different justification for the number of clusters eventually decided upon; Rossow et al. (2005) stated vague criteria, Elsaesser et al. (2010) claimed to have described 60% of the total variance but does not say how, and Jakob and Tselioudis (2003) admitted to deciding the issue "somewhat subjectively." In fact, Jakob and Tselioudis (2003) stated that to their knowledge, "there is no completely objective way of deciding the optimal number and statistical significance of the clusters chosen."

The choices of scene size and $k = 3$ clusters, while made a priori to emulate the method used in Elsaesser et al. (2010), are defensible physically and statistically. As to scene size, a 100km square can be assumed to have fairly homogeneous SST and thus similar properties on the mesoscale; the size is also large enough to contain various cloud types and rain rates, allowing a mesoscale picture to emerge. The clusters show consistency in mean properties from month to month despite cluster frequencies that shift due to seasonal and interannual variability in precipitation.

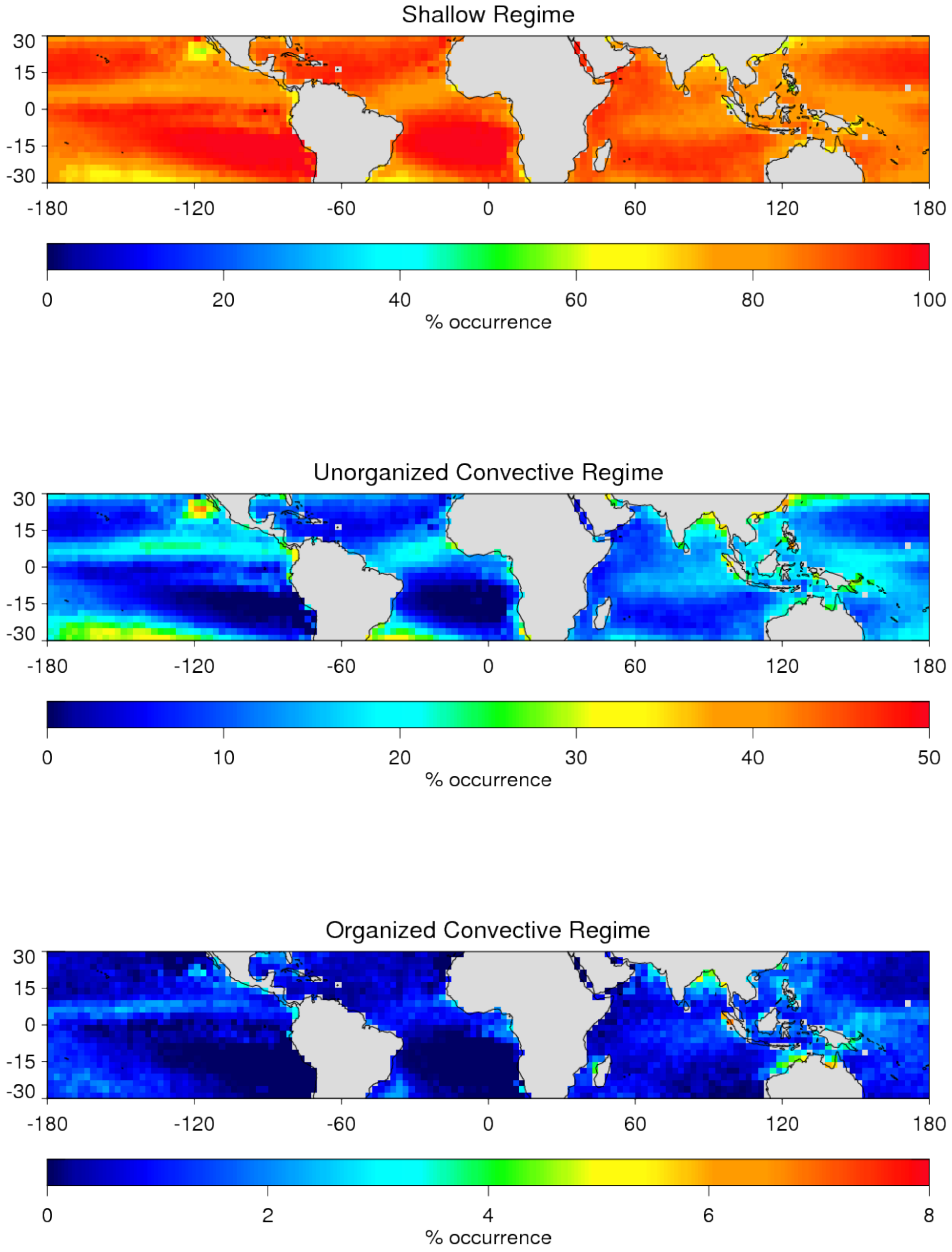

Figure 3.3. Relative frequencies of occurrence for the TMI-derived precipitation regimes from 2003-2006.

A sensitivity analysis, performed for $k = 2$ to $k = 6$ clusters, found that $k = 3$ maximized the between group variance and total variance explained for most months examined. Between-group variance (*bg_var*) is defined as follows, with the number of clusters (*k*) varying in the sensitivity analysis:

$$bg\_var = \frac{1}{k-1}\sum_{cl=1}^{k}\sum_{p=1}^{5}((\bar{x}[cl,p]-x_O[p])^2) \qquad x_O[p] = \frac{1}{N}\sum_{cl=1}^{\#cl}(S[cl]*\bar{x}[cl,p])$$

. Percent of variance explained (*pct_var*) by *k* clusters is defined by the following:

$$pct\_var = \frac{bg\_var}{tot\_var} \qquad tot\_var = \frac{1}{N}\sum_{n=1}^{N}\sum_{p=1}^{5}((x[p,n]-\bar{x}[p])^2)\,.$$

In the given equations, *x* is the array of clustering variables, *p* is the clustering parameter number, *cl* is the cluster number, *N* is the total number of scenes input into the clustering algorithm, *S* is the number of scenes assigned to a given cluster, and $\bar{x}$ signals a mean value.

3.2.4 Consistency and Similarity

The phrase 'self-similarity' is used in Elsaesser et al. (2010) to describe a quality of consistency between elements of a group which have been placed together by some external categorization method. A self-similar group, then, contains elements with a broad similarity, distinct from the general characteristics of elements in other groups. Of course, there are no wholly distinct groups of MCS types in nature; clustering efforts attempt merely to find similar elements in natural processes to elucidate connections that would otherwise be elusive.

The geographic consistency of the TMI-derived deep convective regime is shown in Figure 3.4. Results are divided into the five ocean basins defined in Table 3.1. Scenes co-located with PR provide mean reflectivity profiles for convective and stratiform pixels (an attribute given in the 2A25 product), allowing for direct comparisons between regimes and between scenes from the different ocean basins. In Figure 3.4, mean reflectivity profiles from each scene are shown together by way of a contoured frequency by altitude diagram (CFAD) to show the most frequent reflectivity profile for each basin. Three years of PR data were co-located to match with the TMI scenes.

Some variation exists between basins as, for example, cloud top heights in the Indian Ocean basin tend not to be as high as those in the Atlantic or East Pacific. However, despite some differences in cloud top height especially, the similarity of the regimes between ocean basins is evident. Some basins show cleaner profile distributions than others due to a greater number of available cases. Plots for the other regimes are found in the Appendix (Figures A.1 and A.2).

When co-locating scenes defined by this method with the centers of tracked systems from CMORPH, the tracked systems are identified as the deep convective cluster type 55% of the time. Tracked systems fall into the mid-level and shallow regimes in 43% and 2% of all cases, respectively. This seemingly low percentage of matches with the deep convective regime may be due to the deep convective regime accounting for a mere 1% of all scenes. The method of matching uses all points along the system's track—the first and last time steps often contain cloud systems that are still building depth or have started decaying, for example, dropping into the mid-level classification. The calculated center of a tracked system at a given time step is simply the mean latitude and longitude of all pixels that meet the rain rate threshold; this somewhat simplistic method of geolocation is a possible cause of some difficulties in co-location with other datasets.

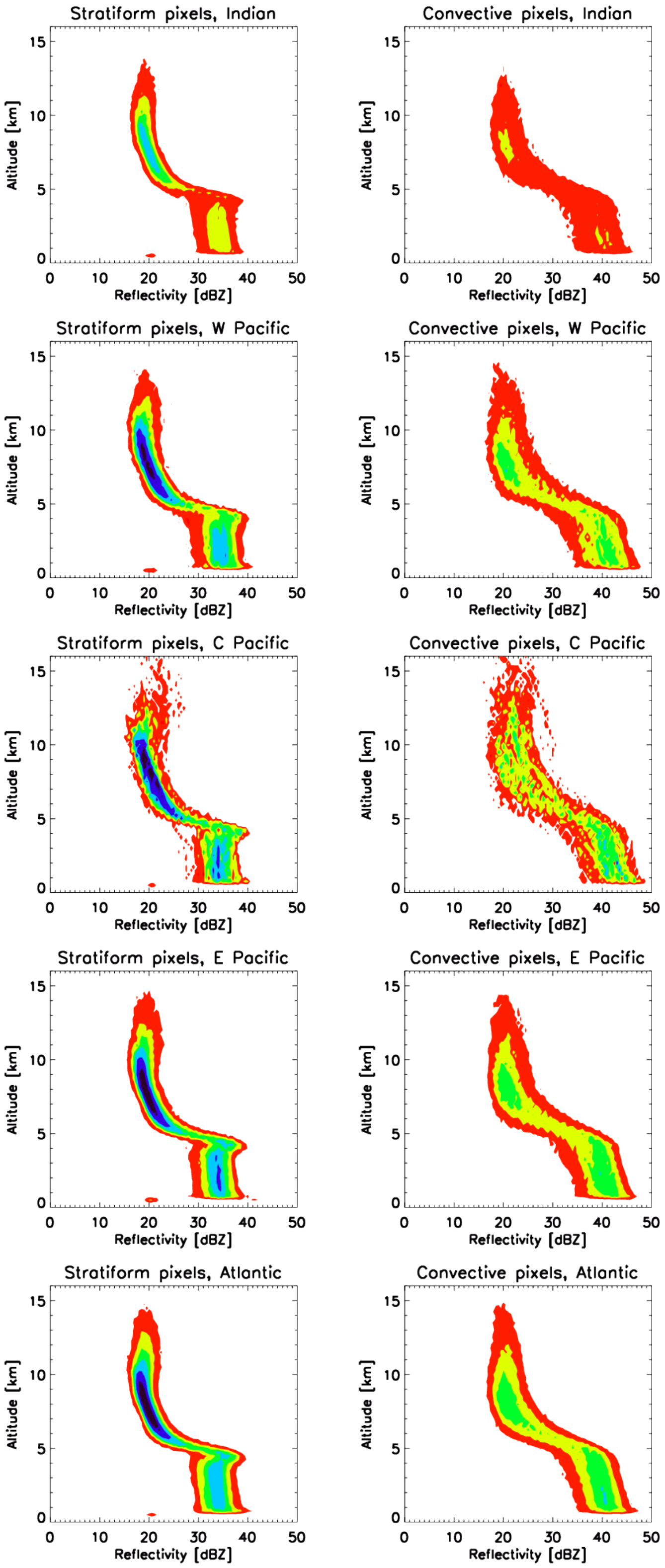

Figure 3.4. Radar reflectivity profiles from PR are shown in contoured frequency by altitude diagrams (CFADs) for the TMI-derived deep convective regime, separated by basin (rows) and convective (right) versus stratiform (left) pixels.

4. ENVIRONMENT

4.1 Introduction

All precipitation events affect the local environment in which they occur. These effects are manifested specifically in variables that comprise the water and energy cycles. In the concept of radiative-convective equilibrium, a radiative imbalance causes an unstable atmospheric temperature profile, inducing convection that acts to stabilize the atmosphere through latent heat release. The water and energy cycles are connected through this constant struggle for equilibrium. Rainfall tends to cool the surface, increase near-surface humidity, and eventually decrease cloud amount among other effects. In Stephens et al. (2004) the different phases of the MJO are connected to the mutual regulation of SSTs and convective activity, linked by the "coupling between the ocean, moist atmospheric thermodynamics, radiation, and the dynamics of the tropical warm pool regions." That study details a complex chain of events, focused around the MJO and radiative-convective equilibrium in the Pacific warm pool, showing the interconnected nature of precipitation, environmental constituents, and large-scale atmospheric dynamics. The environment's response is closely related to the state and characteristics of the raining system, a guiding assumption for the analysis presented in this section. Environmental characteristics and specific effects on local water vapor, evaporation, clouds, radiation, and SST are all explored.

It is intuitive that propagation speed is a large determinant of a system's local impact, given that speed determines the residence time of rainfall and cloud structures in a given area. Slowly moving systems deposit a large amount of rainfall in one locale, with the associated cloud field decreasing the magnitude of solar radiation that reaches the surface, two causes of a drop in SST. Fast systems have less time to make an impact on a specific area, but are also likely driven by different dynamics that can affect wind fields and processes such as LHF and water vapor convergence. System speed is the main point of focus here for contrasting the environmental effects of heavily precipitating MCSs, but other factors such as the ocean basin of occurrence and the different atmospheric dynamics therein clearly show their importance in the results presented.

4.2 Clouds

The evolution of clouds before and after the passage of a precipitating MCS is found to follow a cycle of shallower clouds building to deeper clouds and then dissipating. More specifically, smaller scale convection and scattered cumulus clouds grow into large-scale deep convective clouds before dissipating into smaller deep convection and thick cirrus, then returning back to the mean distribution (Figure 4.1). Fast and slow systems arise from similar cloud types and decay to similar cloud types. This evolution of cloud types from observations is in line with the building blocks concept of the tropical convection lifecycle (Mapes et al. 2005) in that cloud systems appear to follow the same evolution, regardless of the timescale.

The cloud state results presented are composited means due to the daytime nature of the observations, with thousands of cases composited to produce the relatively smooth curves shown. In spite of the inherent daytime bias of the dataset, the results signal that the tracking method is able to capture the lifecycle of large-scale deep convective cloud systems. The smoothness of the curves also suggests that the cloud states do not exhibit much diurnal variability. It should be stressed, however, that the ISCCP cloud regime data are on a 2.5° grid, and thus do not capture smaller scale variability in cloud fields. The ISCCP cloud regimes are defined in Figure 2.2 and Table 2.1.

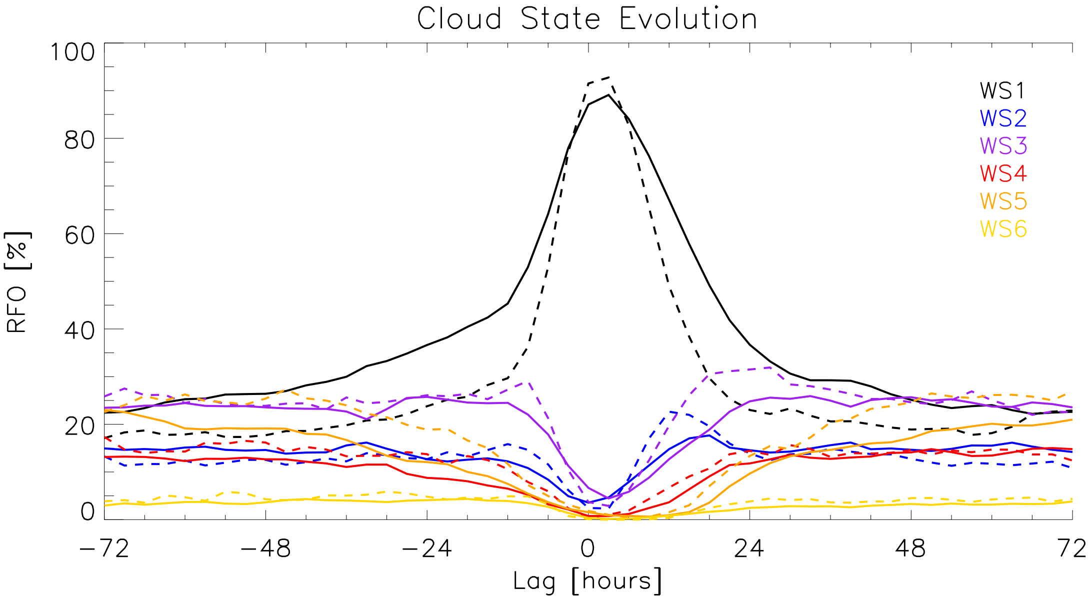

Figure 4.1. Evolution of cloud regimes (defined in Table 2.1) centered at system passage, shown for fast (dashed) and slow (solid) system speeds.

Nearly every tracked system is identified as coincident with the deep convective cloud regime (WS1) in the ISCCP dataset, i.e. at lag time zero. Figure 4.1 shows how WS1 dominates nearest the system's passage with a frequency of occurrence near 90%, while the periods before and after the passage are largely smaller-scale convection (WS3) and scattered cumulus (WS5). This is similar for fast and slow systems, with the main difference being the persistence of WS1. For the fast systems, WS1 is the most likely cloud state for around 24 hours, while WS1 tends to last much longer for slowly moving systems. In fact, WS1 is the most likely cloud state for slow systems for nearly 4 days, pointing to most slow systems being large in scale and persistent. Since most slow systems do not rain solidly for multiple days, there is clearly a separation present between precipitating and non-precipitating deep convective clouds. This corroborates the finding in Lee et al. (2013) that the presence of WS1 does not necessarily imply precipitation, with WS1 exhibiting no rainfall nearly half the time.

Another difference between fast and slow systems' cloud state evolutions can be seen in the higher frequency of occurrence of WS2 and WS3 following the system's passage. WS2 and WS3 are defined as convectively active cloud states that may have more isolated deep convection or convection that is not as strong as in WS1. It makes sense that these weaker convective cloud states are more prevalent after a fast system goes through. The ISCCP clustering algorithm identifies the decaying deep convection as WS2 or WS3 depending upon the distribution of cold cloud tops and optical depth of the remaining cloud system, a more likely outcome following fast systems due to their smaller characteristic size (Table 3.1). There is also a slightly higher frequency of WS5, the scattered cumulus cloud state, for fast systems before and after system passage.

The greater prevalence of the scattered cumulus cloud state before and after fast systems meshes well with Figure 4.2, in that cloud fraction is smaller at nearly every time step for fast systems. This holds true for every basin at every time step apart from at system passage itself, with the Indian Ocean basin at 2-3 days after passage being the lone exception. Slow systems are associated with larger and more persistent cloud fields, a result of greater anvil development and greater system size, making it more likely for their cloud fields to occupy a large percentage of the sky. The plot of cloud fraction demonstrates that there is usually complete cloud cover when a tracked MCS passes through, a good check to demonstrate that the matching with ancillary data is physically reasonable.

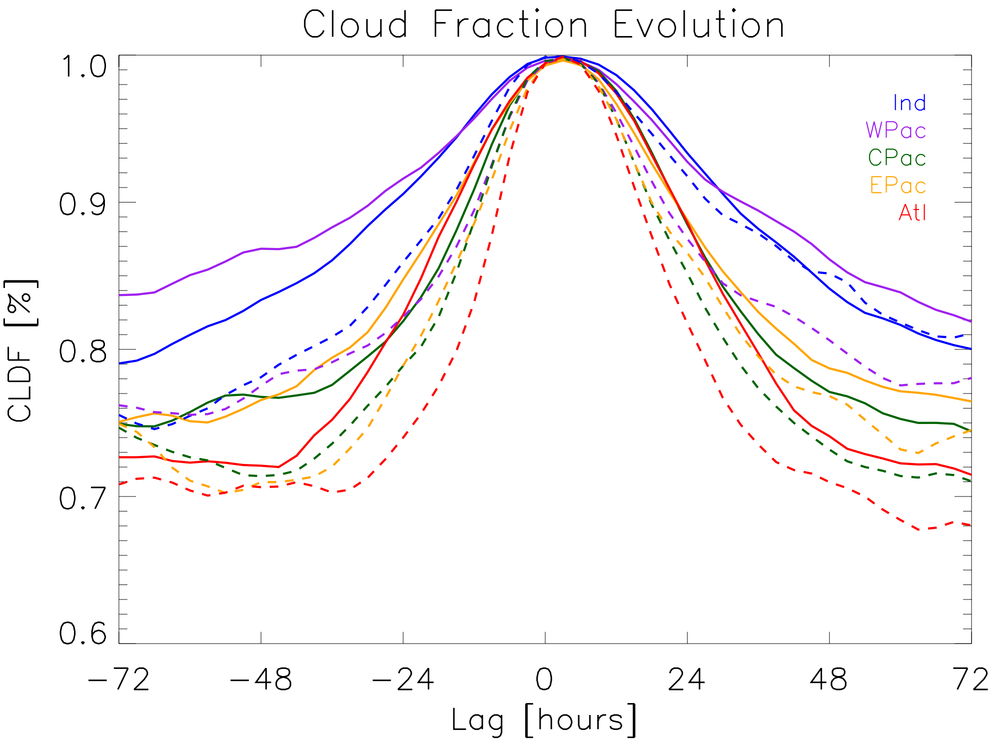

Figure 4.2. Cloud fraction evolution, shown for fast (dashed) and slow (solid) system speeds.

It is interesting to note that cloud fraction appears to peak at 3 hours after the defined system passage. While this could be an insignificant signal (a difference in the mean of around 1%), it does raise compelling questions. Assuming that the matching method and dataset used do not contain systematic biases, a physical explanation of the observed behavior is needed. The SRB dataset is on a 1° global grid, and matching the nearest grid point with the calculated geographic center of the tracked system may mean that the system center is as much as 70km away from the center of the matched grid box. Full development of the anvil cloud of the MCS may lag behind the heaviest rainfall, with the cirrus outflow from the convection fully covering the grid box a few hours after the heaviest rain rates have already occurred. Due to cloud fraction being defined as a percentage of grid box area populated by clouds, this seems a reasonable explanation for certain cases, as even a few scattered cases could affect the mean by a few percent. In spite of the root cause of the slight lag in cloud fraction, these results show certain characteristic differences between system speeds and ocean basins that will be echoed in other results.

4.3 Shear

Examination of wind shear provides a chance to look at a causal factor in the local environment as opposed to an effect due to the passage of an MCS. Analysis of wind shear at the time of system passage shows a key physical difference between fast and slow propagating systems when considering all basins (Figure 4.3). Fast systems generally exhibit stronger wind shear magnitudes in the mid troposphere from 875mb to 500mb. The slow systems show stronger shear near the surface, likely due to a greater influence of cold pools.

The general pattern of shear differences shown in Figure 4.3 holds in all basins except the Central Pacific, where shear profiles are nearly identical for fast and slow systems. The Atlantic basin holds the biggest difference between fast and slow system profiles, with fast systems exhibiting 50-100% stronger shear from 850mb to 700mb. Results separated by basin are found in the Appendix as Figures A.3 and A.4, using different levels (as defined in section 2.4.2) to calculate shear. So, while significant differences exist between basins, the mean wind shear profiles hold a key contrasting physical feature of fast and slow systems. The discrepancy in shear suggests a prescriptive method for examining the behavior of deep convective MCSs in models, as wind fields are a common model output parameter.

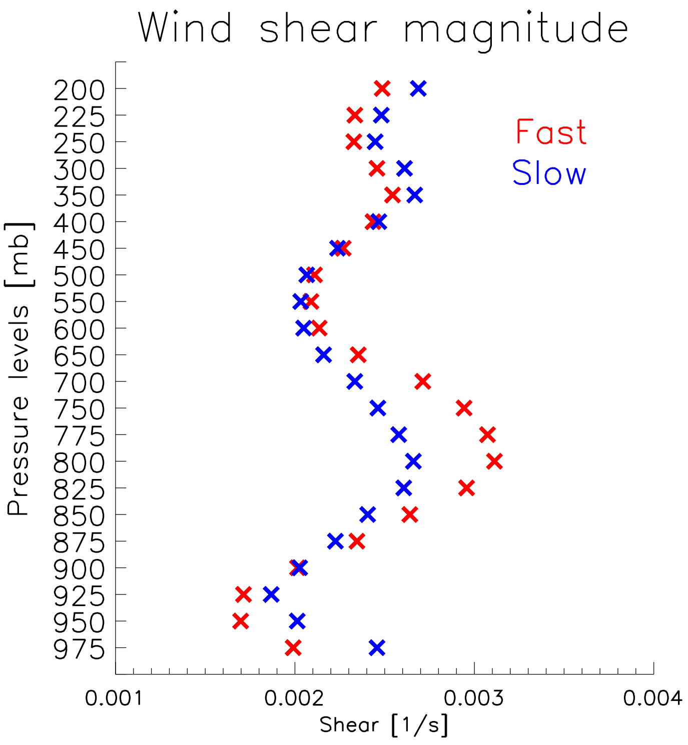

Figure 4.3. Mean wind shear profile for all fast and slow systems. *Lev*=1 as defined in Section 2.4.2.

4.4 Water vapor

The water budget at every point on the globe is comprised of precipitation, evaporation, and changes in water vapor that are characterized by the time derivative of TPW and water vapor divergence as defined in section 2.4.2. These elements have to balance for all spatial and temporal scales,

$$-\nabla \bullet q\vec{v} + \frac{dTPW}{dt} = P - E$$

where P and E are rates of precipitation and evaporation, respectively. Each element of this balance is examined, again centered on passage of the MCS through the area in question. It should be stressed that the above equation is always true in nature; however, it is very difficult to perfectly close the water budget on any scale using observations alone, just as closing the energy budget has proved contentious (Wild 2012; Trenberth et al. 2009; Stephens et al. 2012).

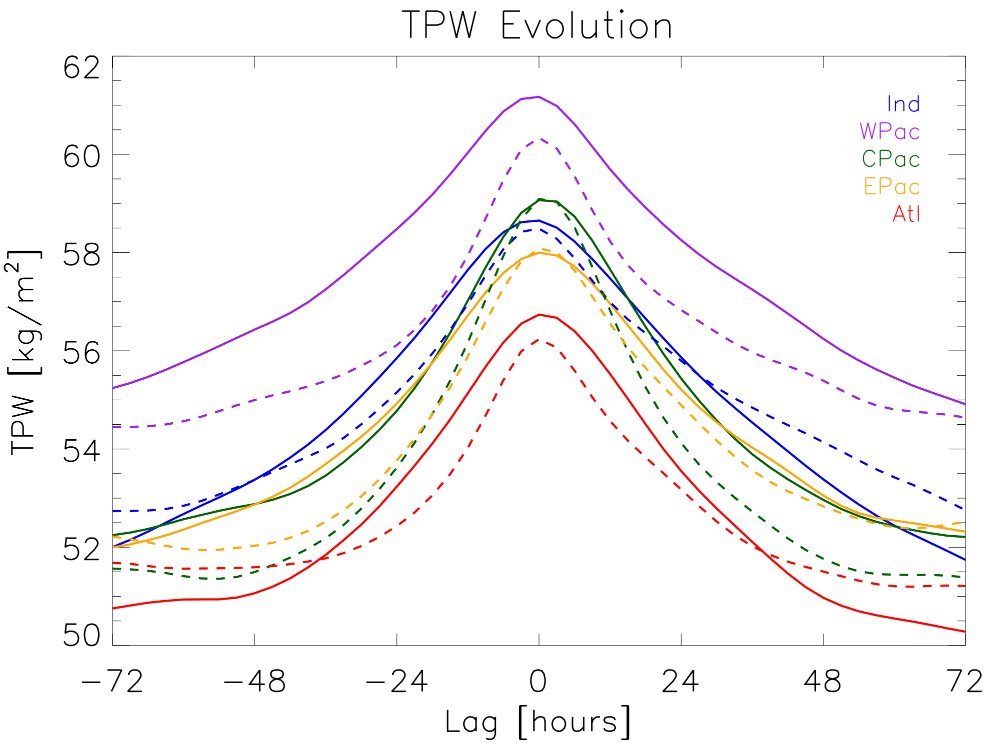

Figure 4.4. Evolution of TPW for fast (dashed) and slow (solid) systems.

TPW is perhaps the best-constrained observational component of the water budget. While this study uses data from reanalysis (ERA-Interim) for TPW, observing TPW from passive microwave sensors is one of the most accurate measurements observed by satellite. The ERA-Interim dataset assimilates observations from myriad sources, with oceanic water vapor coming predominantly from orbiting microwave sensors (Dee et al. 2011). The evolution of TPW around the passage of a tracked MCS is given in Figure 4.4, with mean behavior startlingly similar between basins. This striking similarity in the effect on TPW is evident in Figure 4.5, with the initial value subtracted to illuminate inter-basin behavior. All basins and both fast and slow systems exhibit a peak in TPW at system passage, with TPW at lag 0hrs approximately 6kg/m^2

higher than at lag 72hrs or -72hrs. Great symmetry is visible in these mean curves, notably showing no significant net effect; Figure 4.5 shows the spread in net effect to be within 0.5kg/m^2. This is an important result, signaling that the effect of deep convection on total water vapor is quite transient, similar to a result seen in Masunaga (2012, his figure 6c) despite this study using a different method and focusing on more extreme MCS types; that study found a 4kg/m^2 increase in TPW due to an MCS, versus the 5-7kg/m^2 values seen in Figure 4.5. The main difference seen between fast and slow systems is the rate of TPW increase and decrease, with fast systems causing quicker changes in TPW.

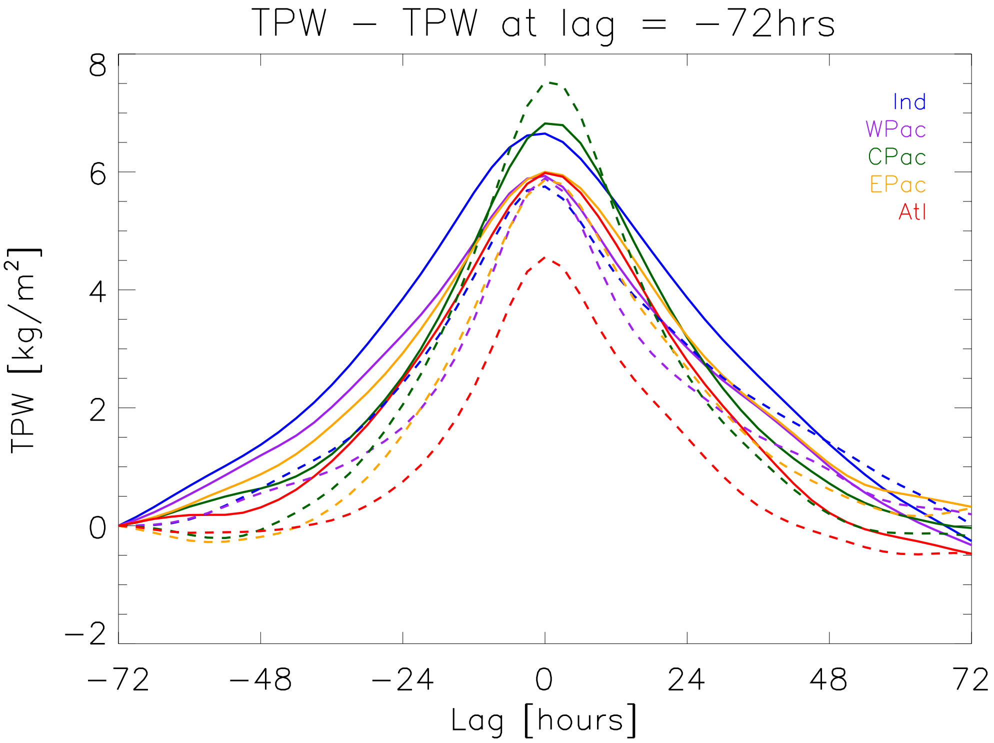

Figure 4.5. Same as Figure 4.4 but with the TPW at lag = -72hrs subtracted.

To gain further knowledge of the changes in water vapor due to MCS activity, the same analysis was performed for water vapor from three segments of the atmospheric column (the surface to 850mb, 850-500mb, and 500-1mb). This analysis is shown in Figure 4.6, using data from all basins for fast and slow systems. The majority of water vapor increase is observed in the middle layer defined, 850-500mb, accounting for about 4mm of the 6mm of total increase in the column. The other key feature of this analysis is that lower-level moisture leads upper-level moisture. Near-surface water vapor peaks around 6 hours before peak rainfall while upper level moisture peaks 3-9hrs after the system has passed, suggesting the persistence of moisture associated with the anvil cloud. Fast systems exhibit a quicker buildup of upper-level moisture and decrease in lower-level moisture after system passage; fast and slow systems are remarkably similar from 850-500mb. These results are consistent between basins, with the main difference being simply the background amount of moisture. Plots showing each basin separately are found in the Appendix.

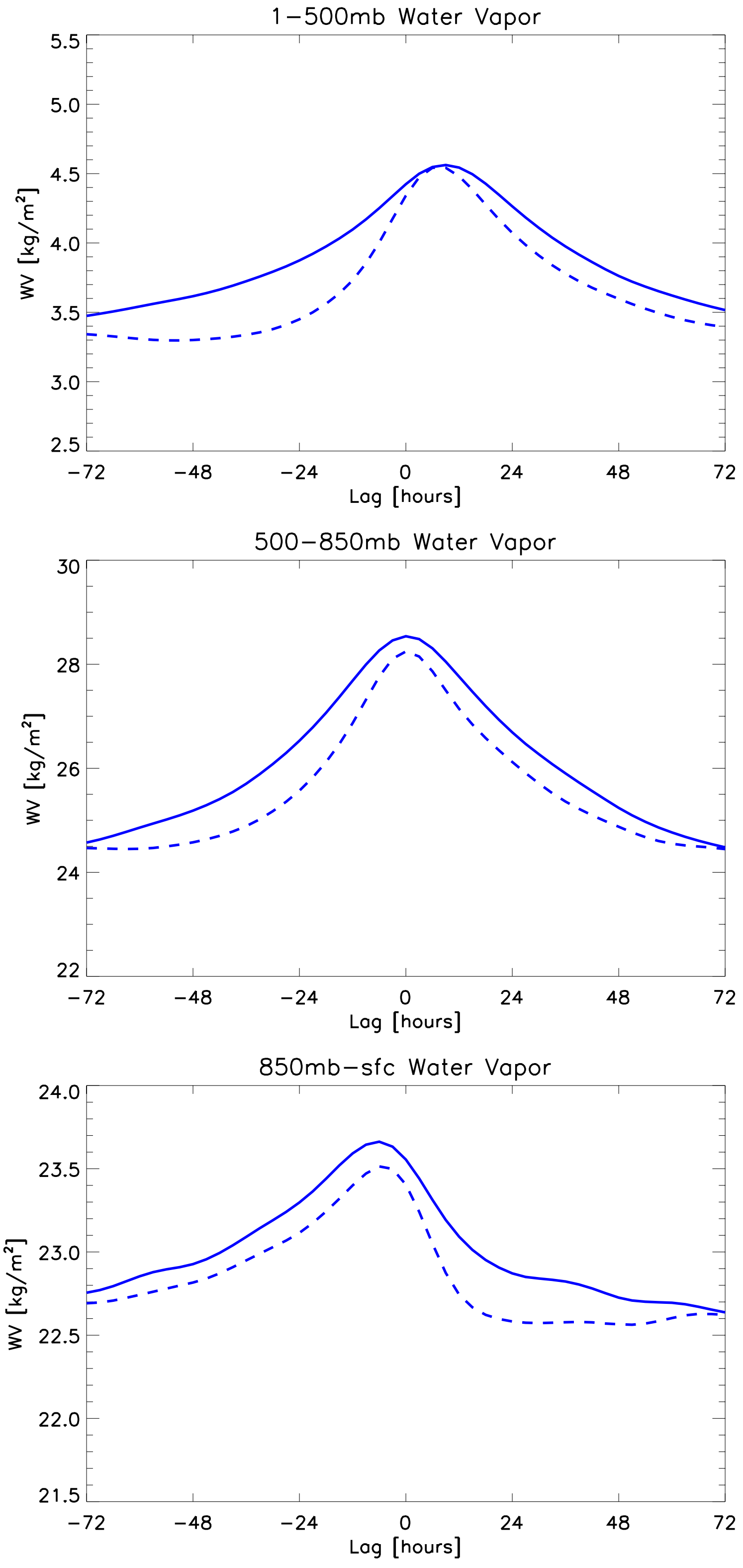

Figure 4.6. Water vapor evolution of fast (dashed) and slow (solid) systems for three vertical segments of the atmosphere: 1-500mb (top), 500-850mb (center), and 850mb-sfc (bottom). Note the different scales.

4.5 Evaporation

Surface evaporation, a rate directly proportional to latent heat flux at the surface, is a fairly constant source of water into the atmosphere in the Tropical Ocean. LHF is dependent on the air-sea humidity difference, near-surface wind speed, and ocean surface roughness (Cayan 1991). The main impact on LHF of a passing MCS will be changes in surface winds that increase ocean surface roughness and thus increase evaporation and decrease SST. The results of LHF analysis are found in Figure 4.7. Comparison with Figure 4.10 shows that mean evaporation vaguely follows the background mean SST in each basin, with the East Pacific and Atlantic having both the lowest mean SST and smallest LHF. Surface temperature is a factor in the air-sea humidity difference, signaling that changes in near-surface water vapor and winds are driving the finer-scale variability for each basin seen in Figure 4.7, though parsing these interdependent influences on the mean LHF evolution is not without difficulty.

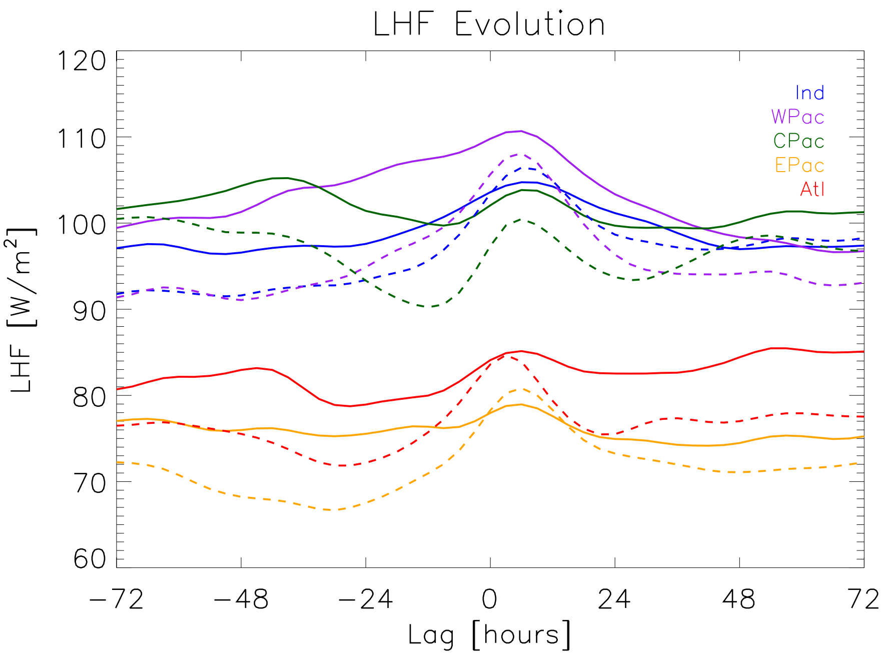

Figure 4.7. Evolution of LHF for fast (dashed) and slow (solid) systems.

In general, slow systems cause greater evaporation before and after system passage. This is likely caused by the larger overall size of slow systems (see Table 3.1), setting up a larger mesoscale circulation and increasing surface wind speeds. Both fast and slow systems exhibit a peak in LHF 6-9 hours after system passage, with this peak being more pronounced for fast systems. This delayed peak in evaporation is coincident with a drop in near-surface humidity, implied in the bottom panel of Figure 4.6, which boosts the air-sea humidity difference and thus evaporation. Slow systems from the Indian and West Pacific basins are slight outliers, with high rates of evaporation but very steady increases and decreases before and after the system. These are the two basins most affected by the large and slowly moving disturbances associated with the MJO, an influence that could be the cause of the smooth mean curves in Figure 4.7.

Another interesting feature is the increase in LHF about two days before and two days after the maximum in LHF that occurs at 6-9hrs lag, seen most clearly in the Atlantic and Central Pacific basins. These features are echoed in the plots of water vapor at lower levels, most easily seen for slow systems in the Atlantic (Figure A.6). The exact cause of these small lower level fluctuations in humidity is unknown. Ascribing direct causality to every feature in Figure 4.7 is difficult, and a more extensive analysis of near-surface wind fields and humidity would be necessary, especially when examining inter-basin differences. The passage of a heavily raining MCS is seen to generally increase evaporation in its wake, but total variability in the mean evolution is within about 10% for each basin. Compared to the changes witnessed in other elements of the water and energy budgets, evaporation is fairly constant when examining all basins together.

4.6 Water vapor convergence

Water budget analysis can be problematic on short time scales, especially given a reliance on reanalysis data. It is known that models and reanalyses do not resolve very heavy precipitation well in the Tropics due to imperfect convective parameterizations (Stephens et al. 2010). Attempts to mix observational datasets with reanalysis datasets, especially on the scale of a single grid box with very heavy precipitation, were therefore not expected to close the water budget. Despite this caveat, water vapor divergence from reanalysis data still provides certain insights into the source of water for heavy precipitation.

As seen in Figure 4.8, each basin shows large-scale water vapor convergence during the 6-day period surrounding the tracked events. Convergence steadily increases until the system's passage, at which convergence peaks at around 0.7mm/hr, then falls sharply to values of approximately 0.2mm/hr. Similar to previously discussed ancillary fields, characteristics of water vapor convergence differ slightly between basins and faster systems show a quicker rise and fall of convergence. All cases show a peak in convergence at 3-6hrs before system passage.

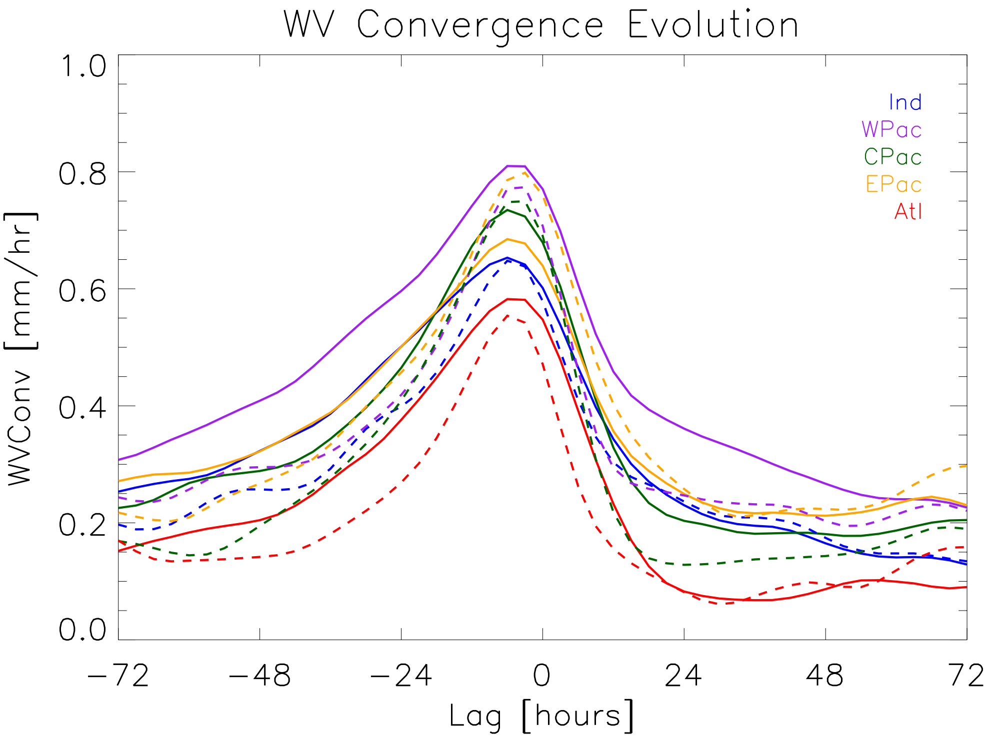

Figure 4.8. Changes in columnar water vapor convergence for fast (dashed) and slow (solid) systems.

This flux of water vapor into the area of deep convection is a key source of moisture for the heavy precipitation, but it is not of sufficient magnitude to match with observed rainfall from CMORPH and close the water budget. Figure 4.9 shows how far away the water budget is from closing for the specific type of case examined in this study; the lines signaling the residual should equal zero, given the water balance equation given in Section 4.4. This particular analysis uses the mean of each field on the resolution of ERA-Interim, hence the rain rates that are less than the tracking threshold. It can be concluded that large-scale water vapor convergence is a common, likely necessary element in the development and sustenance of deep convective precipitating cloud structures. However, the calculated water vapor convergence from ERA-Interim is woefully inadequate to provide enough moisture for extreme precipitation to occur. Proof of this is that the same analysis performed with ERA-Interim products exclusively yields a consistent water budget but much lower rain rates (Figure A.7 in Appendix). So while the results of Figure 4.8 are important to developing an understanding of the effect of deep convective rainfall on the water budget, they are not truly what occurs in nature.

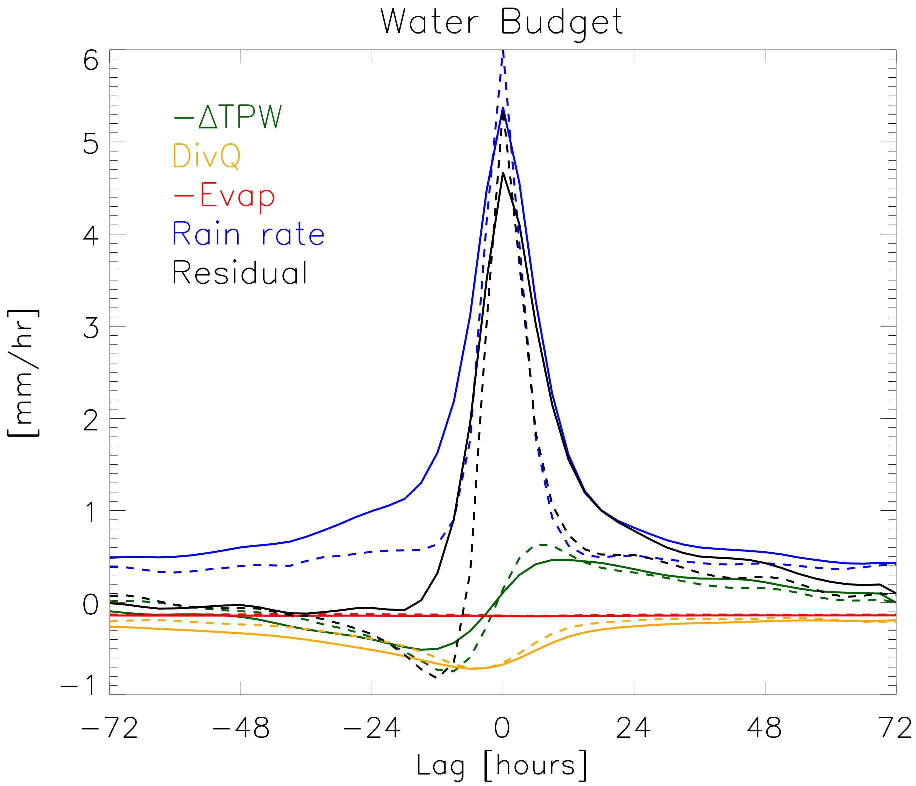

Figure 4.9. Water budget analysis of all systems, fast (dashed) and slow (solid).

4.7 Sea surface temperature

Relatively small variations in SST can have large effects on local and even global weather and climate, as evidenced by the large impact of the El Niño Southern Oscillation (e.g. Trenberth et al., 1997) or the local impact of small-scale SST gradients on the excitation of convection (Li and Carbone, 2012). In an oceanic environment, SST is a key driver of weather variability due to the tremendous amount of available energy stored in the seawater. The ocean surface is an important element of both the water and energy budgets; this section focuses on the observed changes in SST due to MCS activity while attempting to parse out the causes.

Matching changes in SST to the passing of a MCS points to a couple of broad traits and some basin-specific traits (Figure 4.10). The passage of a tracked MCS causes a drop in SST for both fast and slow systems in every ocean basin, with the maximum effect varying from 0.1-0.3°C decrease. As seen most clearly in Figure 4.11, every ocean basin witnesses a smaller mean drop in SST from fast systems than slow systems when looking at the total impact on SST from 72hrs before to 72hrs after system passage. This behavior is quite dependent upon basin, as seen in the difference of SST changes in the Atlantic and Indian ocean basins. The Indian Ocean witnesses net decreases in SST of approximately 0.25°C whereas the Atlantic shows a very small net effect, with fast systems showing virtually no change.

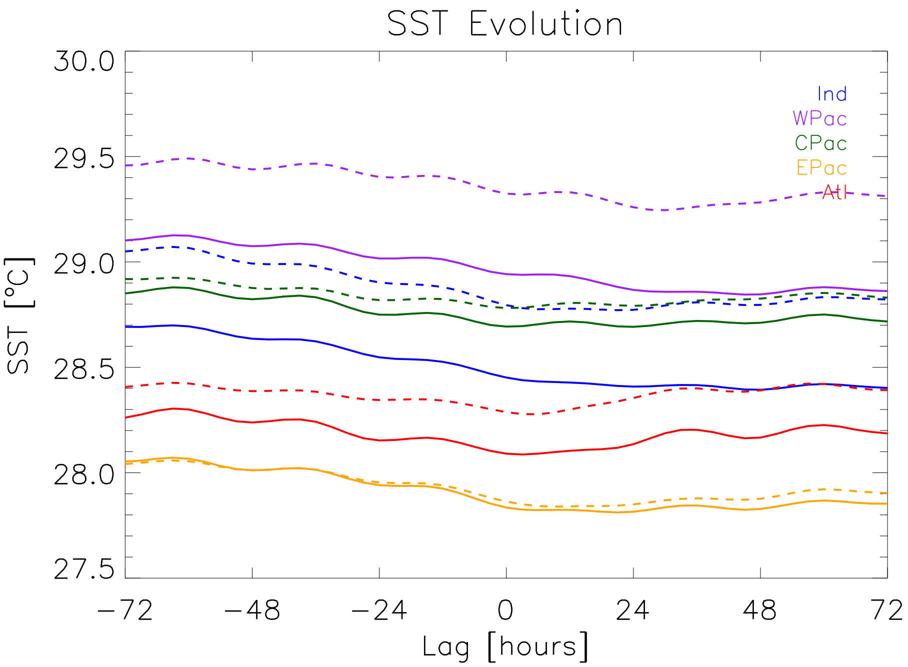

Figure 4.10. Evolution of SST for fast (dashed) and slow (solid) systems.

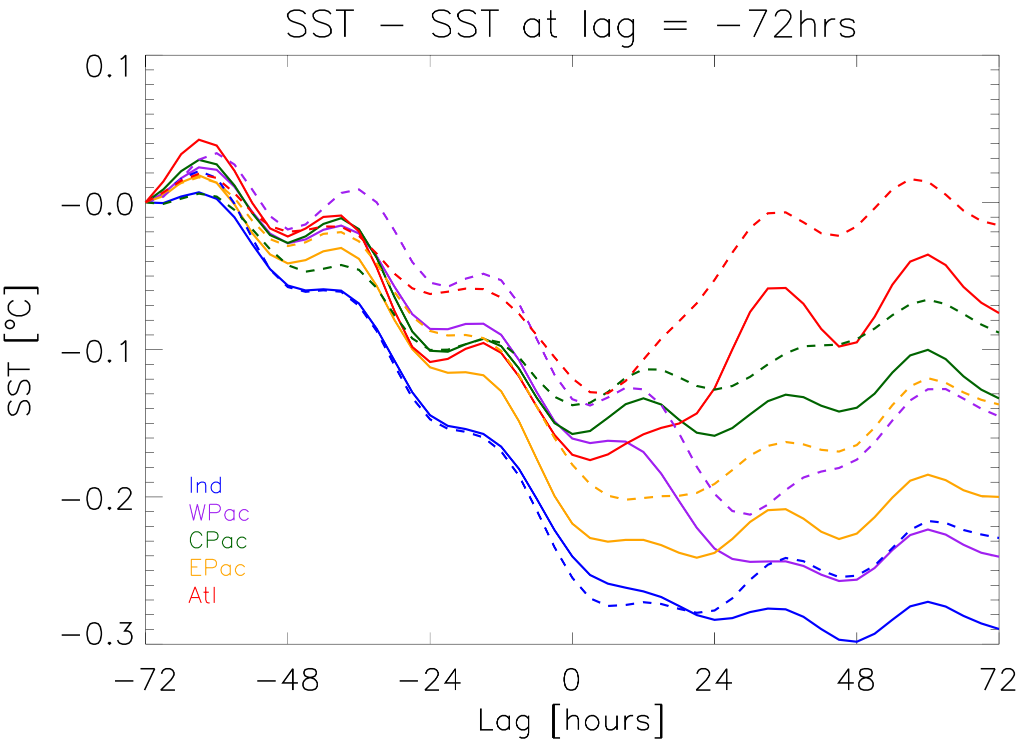

Figure 4.11. Same as Figure 4.10 but with the SST at lag = -72hrs subtracted.

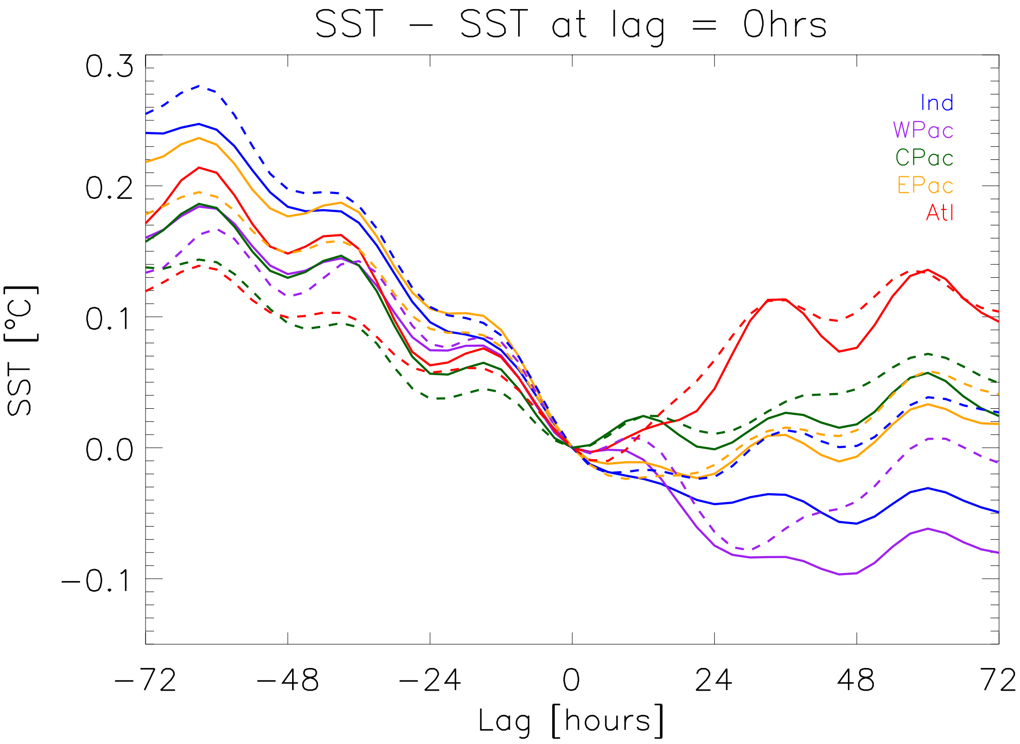

Figure 4.12. Same as Figure 4.10 but with the SST at lag = 0hrs subtracted.

The rate of SST recovery also varies by basin (best seen in Figure 4.12), with system speed being a larger factor in some basins like the West Pacific and Indian than in the Atlantic. A great spread of mean behavior exists between slow-moving systems especially; slow systems in the Atlantic have a net mean drop in SST of 0.09°C while the Indian Ocean's slow systems drop SST by nearly 0.3°C and do not appear to be recovering much even at 72hrs after the defined time of passage. Behavior of the Indian and West Pacific basins appear to be fairly similar, especially for slow systems, a connection that is also apparent in other fields examined. Recovery of SST is highly basin-dependent due to the amount of upper-ocean mixing and differing mixed layer depths (hereafter MLD). If comparing fast systems in the Central Pacific and Atlantic basins, there is a 0.05°C mean difference in SST recovery at 72 hours lag (Figure 4.12), but net radiative flux at the surface is nearly identical. For reference, the Central Pacific has the deepest average MLD at 61.1m while the Atlantic basin is the shallowest annually at 35.0m (de Boyer Montégut et al. 2004). Radiative flux differences play a large role in SST recovery rates, but differences in local ocean dynamics are key for inter-basin variability.

There exists an interesting relationship in which fast systems in most basins occur in higher mean SSTs, seen clearly in Figure 4.10. This is especially true in the West Pacific, with the mean SST for fast systems being 0.35°C higher than that for slow systems. The East and Central Pacific basins do not show this correlation. It seems that this could be a causal factor. The means and standard deviations of latitude are given for each basin and speed in Table 2.1. The West Pacific and Indian ocean basins exhibit the biggest differences in mean SST between fast and slow systems, and also have the most different mean latitudes of all the basins. It is possible that certain latitudes with higher SSTs may tend to witness more equatorial wave activity that drives fast MCSs. While a relationship may exist between higher SSTs and faster systems, this is purely speculative and would require further study to substantiate.

SeaFlux data are derived from a diurnal parameterization applied to the widely used Reynolds SST dataset (Clayson et al. (in preparation)). The Reynolds dataset utilizes infrared measurements of SST in cloud-free conditions and microwave measurements in cloudy conditions (Reynolds et al. 2007), but SST cannot be measured directly by passive microwave radiometer in raining conditions (e.g. Chelton and Wentz 2005). SST in the SeaFlux dataset is necessarily interpolated for time steps in which there is any rainfall, introducing a clear problem for the analysis of SST variability caused by heavily raining systems. To verify the above analysis, in-situ buoy measurements from the Global Tropical Moored Buoy Array are matched with tracked systems (McPhaden et al. 2010).

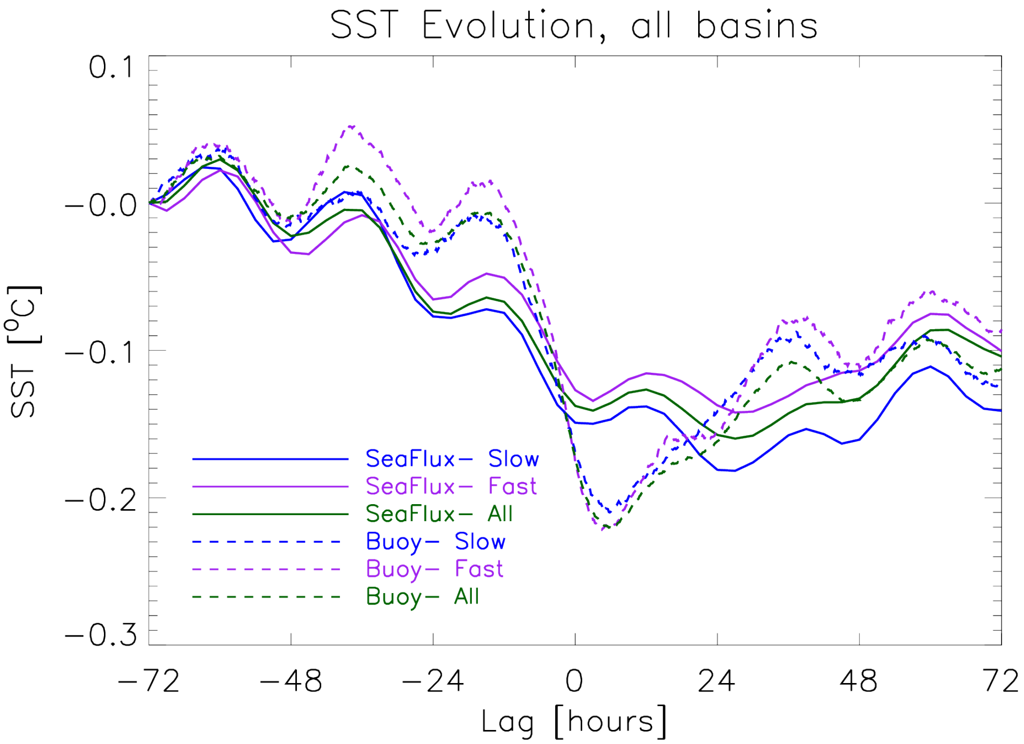

Figure 4.13. Evolution of SST from buoy (dashed) and SeaFlux (solid) datasets.

As seen in Figure 4.13, the in-situ measurements show a much sharper decrease in SST than the composite curves in Figures 4.10-12. These composite curves are taken from moored buoy measurements that are within 1 degree of longitude or latitude of the tracked system's center; the SeaFlux curves shown are only from the cases matched with buoy measurements and therefore differ from the composite curves found for all basins. A majority of the cases matched with buoy measurements are from the Pacific due to the high density of buoys there. The magnitude of the total drop in SST due to passing systems is similar between the buoy-based and SeaFlux composites, approximately 0.23C and 0.17C respectively, but the buoy measurements show a decrease that is both much sharper and recovers much more quickly after system passage. While the analysis of approximately 13000 matched time steps does not permit detailed basin-specific analysis for basins other than those in the Pacific, the following section will demonstrate how closely the buoy-based SST evolution matches the change in surface radiative fluxes and how radiative flux variations are the key driver of observed SST.

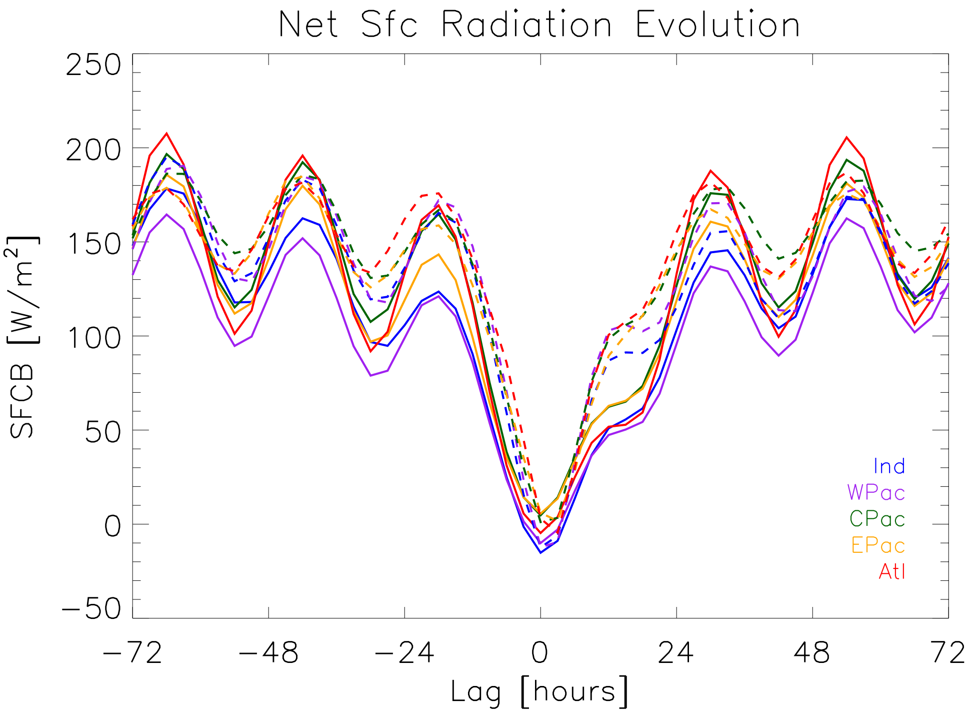

Figure 4.14. Evolution of net radiative flux into the ocean surface, for fast (dashed) and slow (solid) systems.

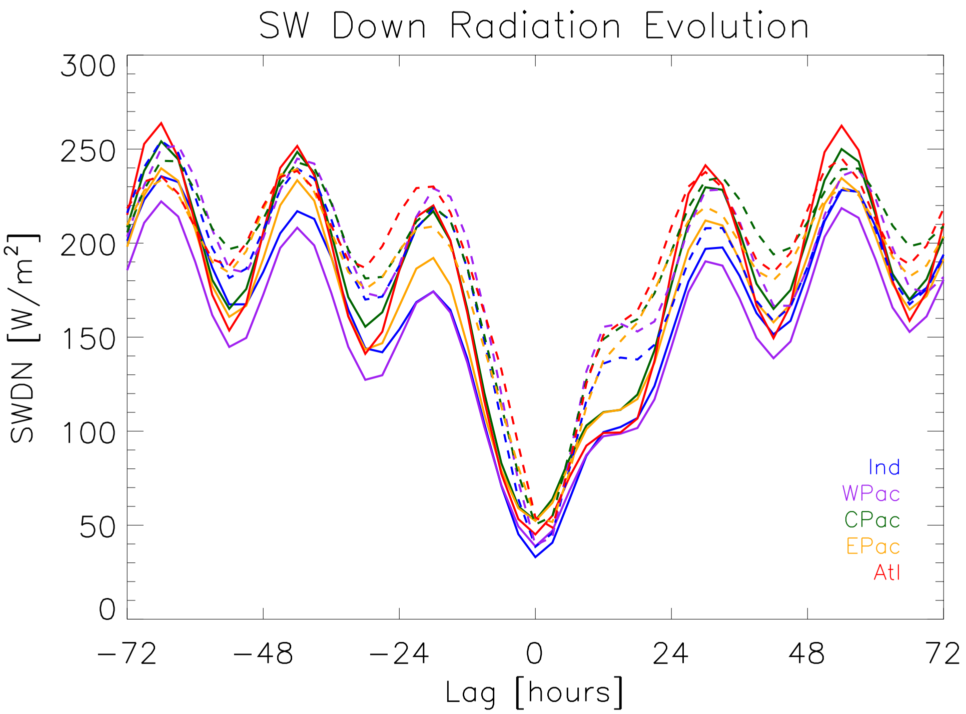

Figure 4.15. Evolution of surface shortwave downward radiation, for fast (dashed) and slow (solid) systems.

4.8 Radiative fluxes

The observed variability in SSTs is caused by a combination of changes in radiative forcing at the surface, evaporation, and accumulated rainfall, though other processes such as oceanic mixing certainly contribute as well. The presence of deep cloud cover causes a drop in solar radiation reaching the ocean surface, manifested by a 190W/m^2 decrease of the net radiative flux into the ocean from mean conditions (Figure 4.14). As seen when comparing Figures 4.15 and 4.14, the variability in net surface radiative flux is almost wholly caused by changes in downward shortwave radiation that reaches the surface, a direct result of the increase in cloud cover and large cloud optical depths.

The sinusoidal look of the curves in Figures 4.14 and 4.15 is caused by the slight diurnal dependence of heavy rainfall in the Tropics (Kikuchi and Wang 2008), with rain occurring preferentially in the early morning; this tendency is shown empirically in Table 3.2, with tracked systems occurring most frequently during 3-6 local solar time. This diurnal signal is also visible in SST variability (e.g. Figure 4.11) due to the diurnal parameterization for SST used in the SeaFlux dataset (Clayson et al. (in preparation)). Changes in LHF (Figure 4.7) have a very small effect on SST, with LHF witnessed to be constant within around 10% and thus a relative non-factor in SST variability, with radiative flux changes on order of 150W/m^2 and LHF changes on order of 10W/m^2.

The other main driver of the decrease in SST is the rainfall itself. The extent to which rainfall actually cools the surface is difficult to estimate because, among other factors, the rain's temperature, the ocean mixed layer depth, and the drop size distribution are variable (Katsaros and Buettner 1969). Assuming that raindrop sizes are not very large, the wet-bulb temperature at the surface is a good approximation of the rain's temperature as it reaches the ocean's surface (Gosnell et al. 1995). Observational evidence from the TOGA-COARE field campaign (Webster and Lukas 1992) showed a generally very small sensible heat flux out of the ocean due to rainfall of 2.2W/m^2, but values greater than 200W/m^2 have been observed coincident with extreme rain rates in the West Pacific. In one instance, a rain rate of 36mm/hr was equivalent to a sensible heat flux out of the ocean of 213W/m^2 (Gosnell et al. 1995). Sensible heat flux due to rainfall can therefore be an important driver of SST variability in extreme cases, but the magnitude of radiative flux changes are almost always larger and longer-lived.

Comparison of the evolution of surface radiative fluxes with in-situ SST measurements clearly demonstrates in the importance of radiation on SST variability. Figure 4.16 shows the mean composite evolution of net surface radiative flux for slow and fast systems in all basins, plotted alongside buoy measurements of SST matched with fast and slow systems that pass within 1 degree of latitude and longitude. Surface radiation leads SST by about 6 hours, with the curves matching up exceedingly well, especially when compared to the SeaFlux-based SST plots which suffer from interpolation issues discussed in the previous section. To show the instantaneous effect of radiative fluxes on SST, Figure 4.17 is a plot of SST tendency, the first time derivative of SST, with the net surface radiative flux for all systems. Basically no lag exists in the relationship between SST tendency and radiation, though the mismatch in time resolution, 3-hourly for flux data versus every 10 minutes for most of the buoy data, hampers any fine-scale analysis of that relationship.

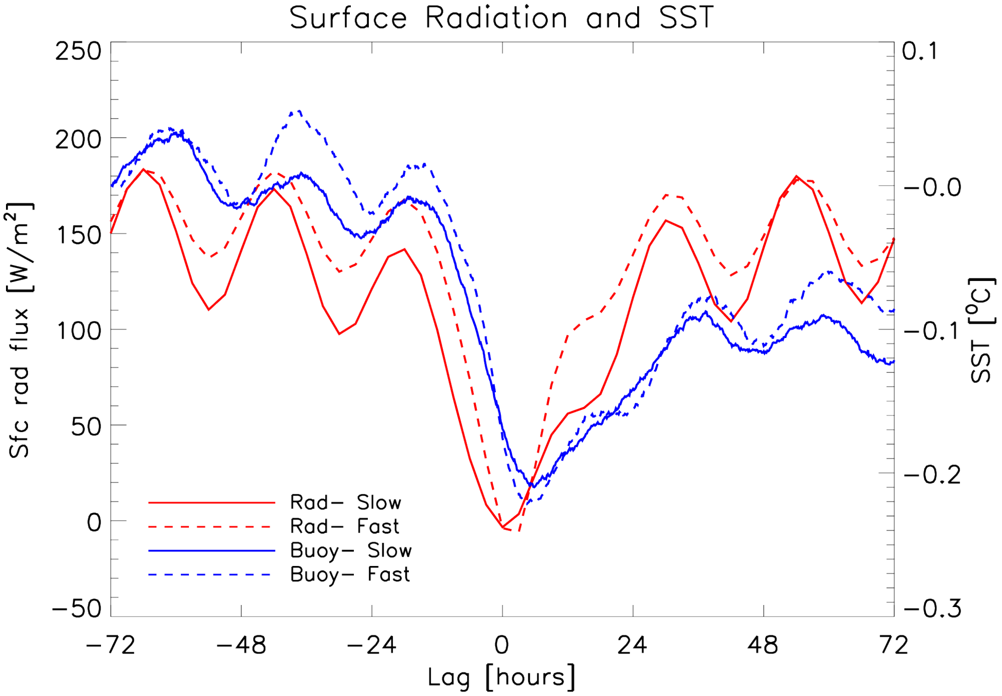

Figure 4.16. Radiative fluxes and buoy-derived SSTs for fast (dashed) and slow (solid) matched cases.

A simple scale analysis proves that changes in the net radiative flux are the main driver of SST when a heavily raining system passes. An estimate of the sensible heat flux out of the ocean due to rainfall is made (following Gosnell et al. 1995), with the broad assumption that a 1mm/hr rain rate scales with ~6W/m^2 in sensible heat flux; the total sensible heat flux is an order of magnitude smaller than the radiative flux. Using a simple formula in which SST is assumed to be the mean ocean temperature at all depths in the mixed layer, an equivalent MLD can be calculated:

$$MLD_{calc} = \frac{\int (\overline{E_{sfc}} - E_{sfc})dt}{C_w \rho_w \Delta T},$$

where C_w is the specific heat of seawater, ρ_w is the density of seawater, and the departure of net radiative flux from the mean is integrated over time. With the time mean of net radiative flux calculated to be approximately 190W/m^2, and integrating over the period of greatest SST decrease, from -18hrs to 6hrs lag, MLD is found to be 13.2m for radiation alone and 15.0m if including a rough estimate of sensible heat flux as well.

The calculated MLD of 15m is significantly shallower than the annual mean MLD in the Tropics of approximately 40m (calculated using data from de Boyer Montégut et al. 2004). The discrepancy is due to three reasons: the short timescale, the mixed layer's inhomogeneous temperature profile, and the rate of vertical mixing. The relatively short timescale of one day does not allow for the entire column of the mixed layer to drop uniformly in temperature because vertical mixing in the ocean is far from instantaneous. Furthermore, the definition of MLD used in de Boyer Montégut et al. (2004) is the depth at which ΔT from the near-surface is 0.2°C, and thus the mixed layer is thermally inhomogeneous by definition. Vertical mixing is also the cause of SST recovering faster after system passage than radiation alone would dictate. This is especially apparent in Figure 4.17, with the tendency in SST becoming positive about 6hrs after system passage despite net radiative flux remaining depressed. Deeper water in the mixed layer aids to stabilize the upper ocean temperature through turbulent mixing. Integrating from -18hrs to 36hrs, a longer timescale to permit further mixing, yields a calculated MLD of 45.8m; this is close to the observational value of MLD and appears to justify the assumptions of the scale analysis.

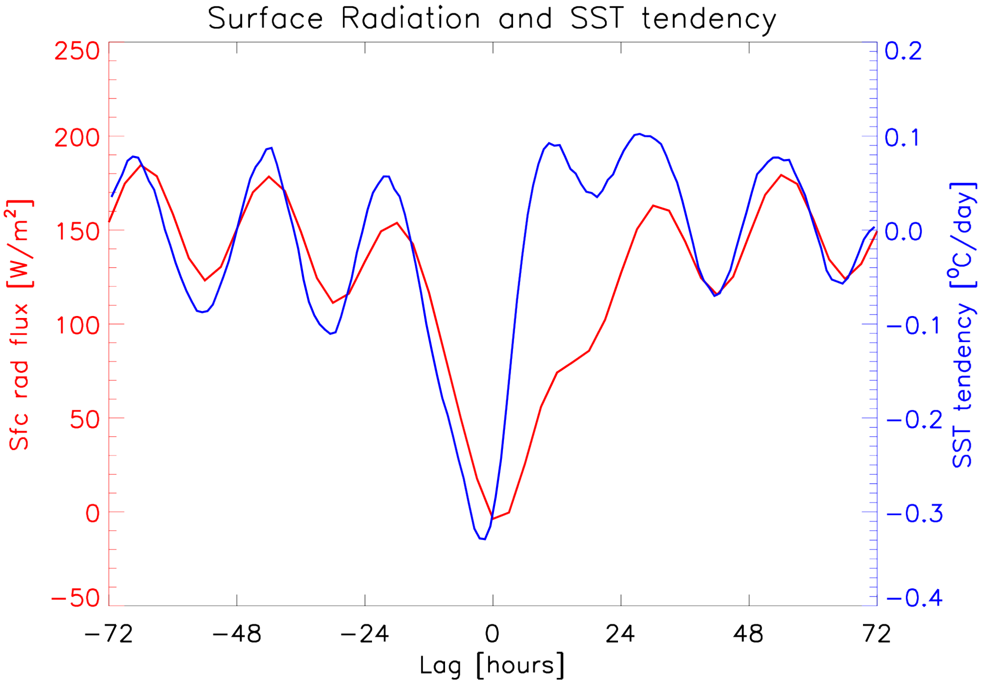

Figure 4.17. Net surface radiation and buoy-derived SST tendency for all systems.

Lastly, the evolution of outgoing longwave radiation at the top of the atmosphere (OLR) is shown in Figure 4.18. Many studies (Arkin and Ardanuy 1989; Wheeler and Kiladis 1999) use OLR to track deep convection and even estimate rainfall, so it is unsurprising to find low OLR values coincident with the heaviest rainfall in all basins and at all system speeds (see Figure 3.1 for an example). Clouds near the tropopause are very cold, emitting less longwave radiation than lower clouds due to the dictates of the Stefan-Boltzmann law of blackbody radiation, and thus OLR is a valuable proxy for deep convection.

The Indian and West Pacific basins contain the highest average cloud tops, with OLR results somewhat mirroring the mean SST in each basin from Figure 4.10 due to higher SSTs being more likely to support strong convection. The persistence of the minimum in OLR is connected to the peak in cloud fraction (Figure 4.2), though high cloud fraction lasts longer than the very cold cloud tops associated with strong deep convection, since clouds at all levels contribute to cloud fraction. Differing widths of the negative spike in OLR correspond to the persistence of very high cloud tops in the area of heavy convective rainfall, again showing slow systems to be associated with larger and/or more persistent cloud fields.

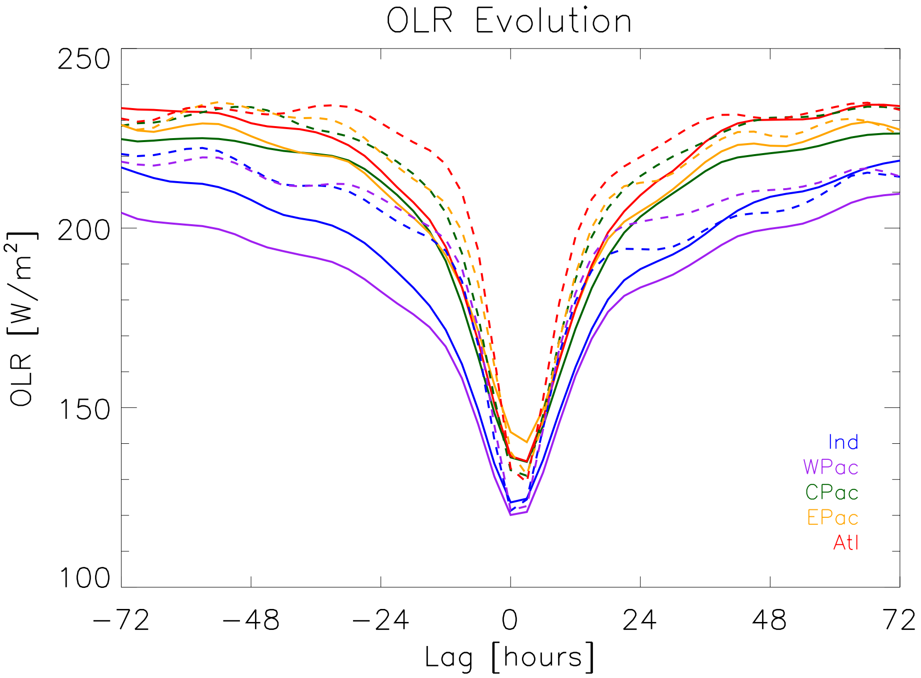

Figure 4.18. Evolution of OLR at the top of atmosphere, for fast (dashed) and slow (solid) systems.

5. FEEDBACKS

5.1 Introduction

The environmental effects catalogued thus far—effects on clouds, water vapor, evaporation, SST, and radiative fluxes— are interdependent and occur on similar time scales. Changes in the environment feed back upon other processes in the atmospheric system, such as how lower-level water vapor variability affects evaporation, perhaps affecting subsequent rainfall and convective activity. The most important possible driver of a feedback on rainfall is SST variability. Relatively small-scale SST gradients have been shown to excite rainfall in the western Pacific, with the relationship between an SST gradient and the onset of convective rainfall highly dependent on background SST (Li and Carbone 2012).

SST decreases due to the passage of a precipitating MCS, at rates dependent upon system speed and ocean basin. The recovery rates of SST (Figures 4.12 and 4.13) especially might affect ensuing convection, with a slow recovery rate aiding to decrease the probability of heavy rainfall in the system's wake until SST can recover. Alternately, an area with persistently depressed SST could aid the formation of nearby convection due to the SST gradient it fosters. While other factors could affect a possible speed-dependent feedback on precipitation, SST is assumed to be the most important factor affecting differences in the recurrence of rainfall.

The method used to explore this possible feedback is fairly simple. At every point in time and space co-located with a tracked MCS, rain rates are collected for subsequent time steps and stored. These rain rate values are from the nearest CMORPH pixel and are thus rain rates from a quarter degree box only, not any sort of scene average. Collected rain rates are put into bins of 1mm/hr intervals, from 0mm/hr to rates greater than 12mm/hr. All the data are then composited together to calculate a probability density function (PDF) of rain rates from system passage itself to 36 hours or 120 hours after passage. This analysis is presented for fast and slow systems and separated by ocean basin as in the previous analyses.

5.2 Rain rate feedback

Short-term feedbacks in precipitation after the passage of fast and slow systems are explored in Figure 5.1, a contoured view of the PDF of rain rates after system passage. These results use data from 2003 through 2006. By design, rain rates of greater than 7mm/hr are most likely at system passage (i.e. at 0hrs), then decline exponentially in probability as time moves forward. At time 0hrs, rain rates of greater than 7mm/hr account for 71% of all cases of both fast and slow systems. At 12hrs this changes to 9% and 2% for fast and slow systems, respectively; at 36hrs after passage the probabilities drop to 2.4% and 1.5%. At a time of 6hrs after the defined system passage, the most common rain rate for both fast and slow systems is 0.01-1mm/hr, with 1.01-2mm/hr being next common.

It is not until 15hrs that the most likely rain rate for fast systems is actually 0.0mm/hr, defined in the CMORPH dataset to be completely non-raining. For slow systems this does not happen until 24hrs. While a period of stratiform rainfall following heavy convective rainfall matches with accepted conceptual models of MCS structure, the prevalence of very light rain rates warrants some skepticism. CMORPH employs 30min, 8km resolution data to arrive at the 3-hourly and quarter degree resolution product used in this analysis (Joyce et al. 2004). The averaging of many rain rate estimates could cause instances of unrealistically small rain rates, and ultimately less instances with a rain rate of zero.

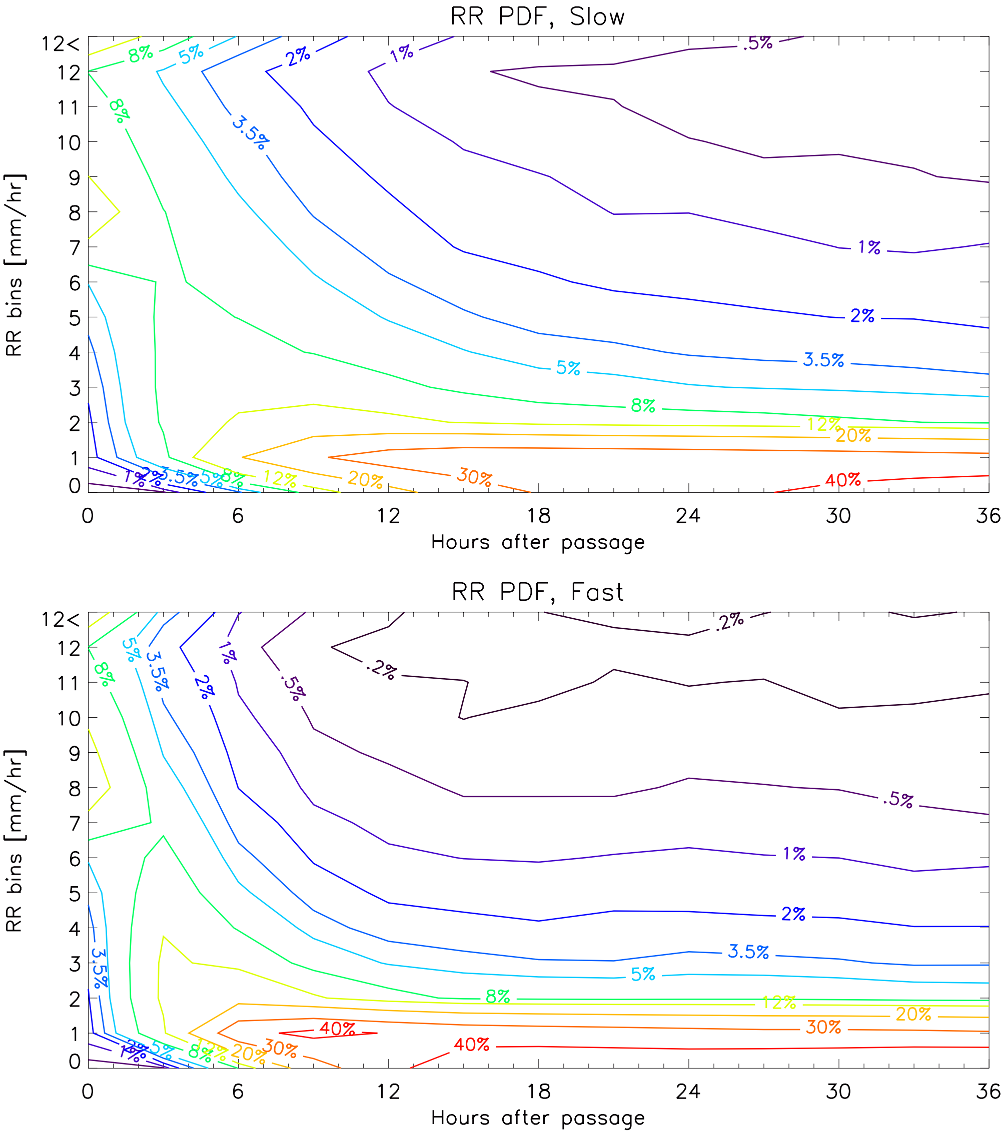

Figure 5.1. Contoured PDF of rain rates following passage of slow (top) and fast (bottom) systems. The PDF at each time step sums to 100%.

Similarly, the output of microwave retrievals such as GProf can include unrealistically small rain rates, an artifact of the Bayesian method employed (Kummerow et al. 2011). The Bayesian retrieval calculates an average of the rain rates applicable to the SST and TPW regime to which each pixel belongs, sometimes yielding unphysical rain rates for pixels that may or may not be raining. Proof of this artifact is that over 4 years of CMORPH data, ~7% of the Tropical Ocean (15°N-15°S) shows a rain rate of 0.1mm/hr or less, with ~2% at exactly 0.01mm/hr

(Table 5.1). CMORPH claims that ~21% of the world has a non-zero rain rate at any given time. Thus, almost half of the precipitating area of the world has one of these tiny rain rates according to the CMORPH product; for comparison, TRMM PR has a minimum detectable rain rate of approximately 0.5mm/hr (W. Berg 2013, personal communication). While very light rain rates do exist in nature, they are not that widespread; most in the dataset are caused by the inability of retrievals to determine very light rainfall unambiguously. However, in spite of this caveat regarding low rain rates in the dataset, there is still a clear difference between fast and slow systems in the prevalence of light rain following the passage of an MCS.

Table 5.1. Frequency of rain rates from CMORPH, 2003-2006, 15°N-15°S ocean only.

RR=0.0	RR=0.01	.01<RR≤0.5	0.5<RR≤1	1<RR≤2	2<RR≤3	3<RR≤4	4<RR≤5
80.76%	2.06%	10.92%	2.19%	1.82%	0.84%	0.48%	0.30%
5<RR≤6	**6<RR≤7**	**7<RR≤8**	**8<RR≤9**	**9<RR≤10**	**10<RR≤11**	**11<RR≤12**	**RR<12**
0.19%	0.13%	0.09%	0.06%	0.05%	0.03%	0.03%	0.06%

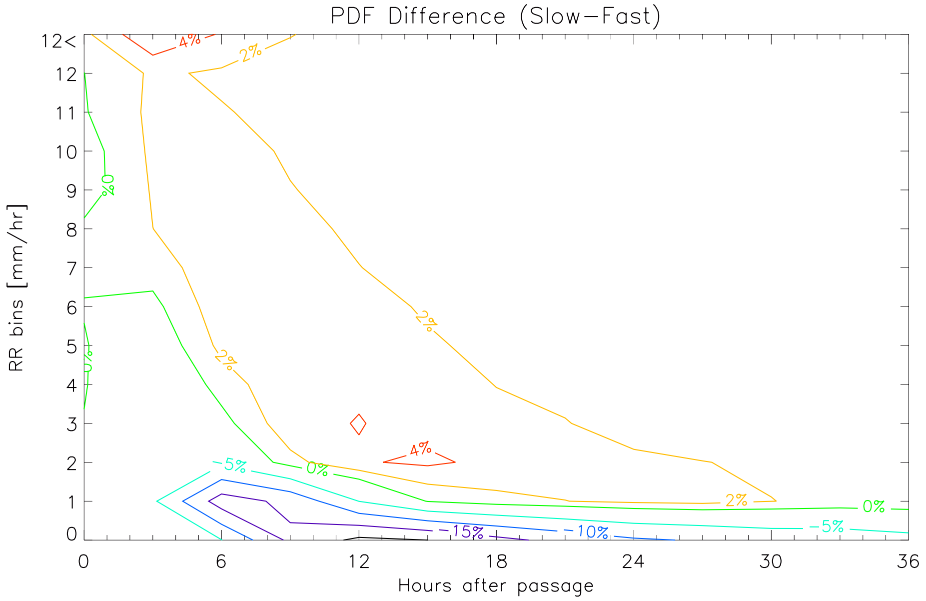

Figure 5.2. Difference of the top and bottom panels of Figure 5.1, representing the Slow PDF subtracted by the Fast PDF of rain rates. This difference of PDFs sums to 0% at each time step.

Locations affected by fast and slow systems both return to something resembling a steady state distribution of rain rates within 36 hours. The fast system cases generally reach this state at about 15 hours while the slow system cases reach it around 30 hours after system passage. These differences are more clearly seen in Figure 5.2, with PDF differences contoured. At 36hrs there is very little difference between the rain rate distributions, with only a slightly greater likelihood of a zero rain rate for fast system cases and rain rates of 1mm/hr or greater a little more common for the slow system cases.

Many of the features visible in Figure 5.2 are simply due to the speed and size of the systems studied and not to any sort of feedback based on something like suppressed SST. The general shape of the differences shows that locations affected by slow moving systems tend to retain higher rain rates for a few hours more than those of fast systems, with slow systems especially exhibiting an extended period of more moderate rain rates. There is also a higher likelihood of very high rain rates persisting due to a slow system. Slow systems are generally larger in area than fast systems by a factor of 2 or 3 (Table 3.1). The average slow system moves at 1.3m/s, about 14km in a 3-hour period, and thus takes a long time to fully pass through a quarter degree box if it has not already rained out and dissipated. These simple differences appear to account for most of the features seen in Figure 5.2, with the higher likelihood of small rain rates from slow systems caused by a larger stratiform rainfall region from the generally larger cloud fields associated with slowly propagating systems.

Figure 5.3 echoes Figure 5.2 but uses a different method for showing differences, with the difference of PDFs divided by the Slow PDF to provide percent differences. Positive values denote rain rate bins more often reached by locations following a slow system, and vice versa for fast systems. However, as seen clearly in the earlier analysis of changes in SST due to fast and slow systems, there is a large amount of variability in SST between ocean basins. A feedback that is assumed to be largely dependent upon SST should be explored via analysis separated by basin. Figure 5.4 separates the analysis of Figure 5.3 by basin using the same contouring method, showing the more significant differences in the recurrence of rain rates. Unaltered PDF plots, like Figure 5.1 but separated by basin, are available in the Appendix (Figure A.8).

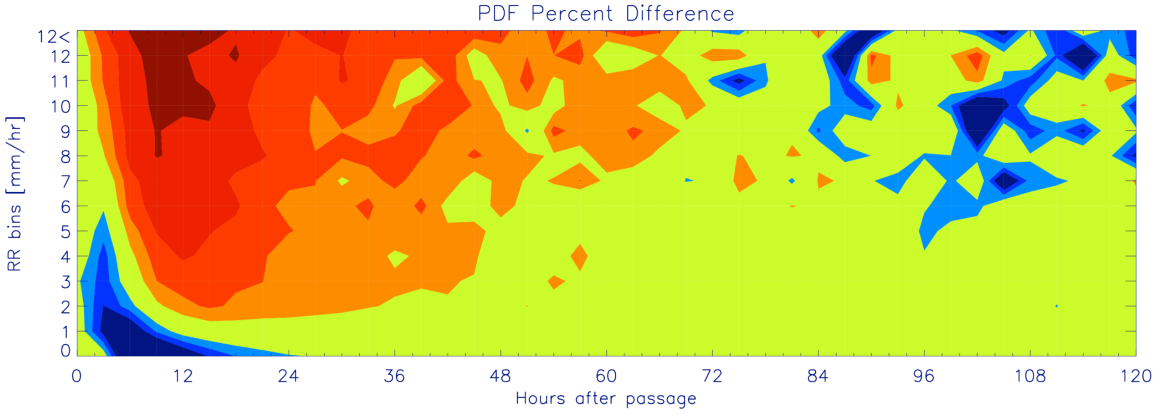

Figure 5.3. PDF differences for all basins combined, shown as a percent difference. Positive (negative) percentages represent slow (fast) systems being more prevalent in that bin. Green represents an equal chance (-20% to 20%), with warm and cold contours at 20% intervals for positive and negative percentages, respectively.

The above figure shows no clear speed-dependent feedback on rainfall. Not until after 84hrs is there any appreciable region on the PDF that shows a tendency towards favoring fast systems. Light and moderate rain rates show a complete lack of signal when looking at all basins together, while heavy rain rates appear to be slightly more likely for locations affected by fast systems in the range of 3-5 days after passage. A key feature of Figure 5.3 is the persistence of moderate and heavy rain rates due to slow systems. Comparing this plot with Figure 5.4 illuminates which basins are responsible for certain features. The Indian and West Pacific basins especially exhibit persistent rainfall features associated with slow systems; this tendency could be related to the Madden-Julian Oscillation (MJO), a slowly moving tropical disturbance that affects convective activity in the Indian Ocean and West Pacific on a 30-90 day frequency (Madden and Julian 1994). Tropical cyclones could also play a role in some of these differences, as the tracking algorithm has no way of differentiating between MCSs and tropical cyclones, and they would also be slowly moving sources of high rain rates. The prevalence of high rain rates 3-5 days after fast systems could be due to the periodicity of certain equatorial wave types that tend to cause fast systems in the first place. Oceanic mixing will generally not allow SSTs to remain significantly depressed more than a couple of days after the passage of an MCS unless there is a particularly large ‘freshwater lens’ that has formed due to heavy rainfall (Schrage and Clayson 2003).

The panels of Figure 5.4 show a certain amount of noisiness at moderate and heavy rain rates, but fairly equal PDFs at low and zero rain rates. Essentially, the difference in PDFs reaches a fairly stable, steady state distribution of rain rates at a slightly different time in each basin. These distributions are marked by nearly identical values at very low rain rates with more variability and noise at high rain rates due to the low frequencies of high rain rates, shown in Table 5.1. Given the hypothesis that differences in SST between locations affected by fast and slow systems will be the biggest driver of variations in rain rate feedbacks, it is expected that the Central Pacific basin would show the smallest signal while the others should be similar (Figure 4.11). However, the Atlantic and Central Pacific basins are quickest to exhibit a greater prevalence of high rain rates for locations affected by fast systems (Figure 5.4). This result points to the importance of other influences on the recurrence of rainfall beyond the drop in SST associated with passing deep convective cloud systems.

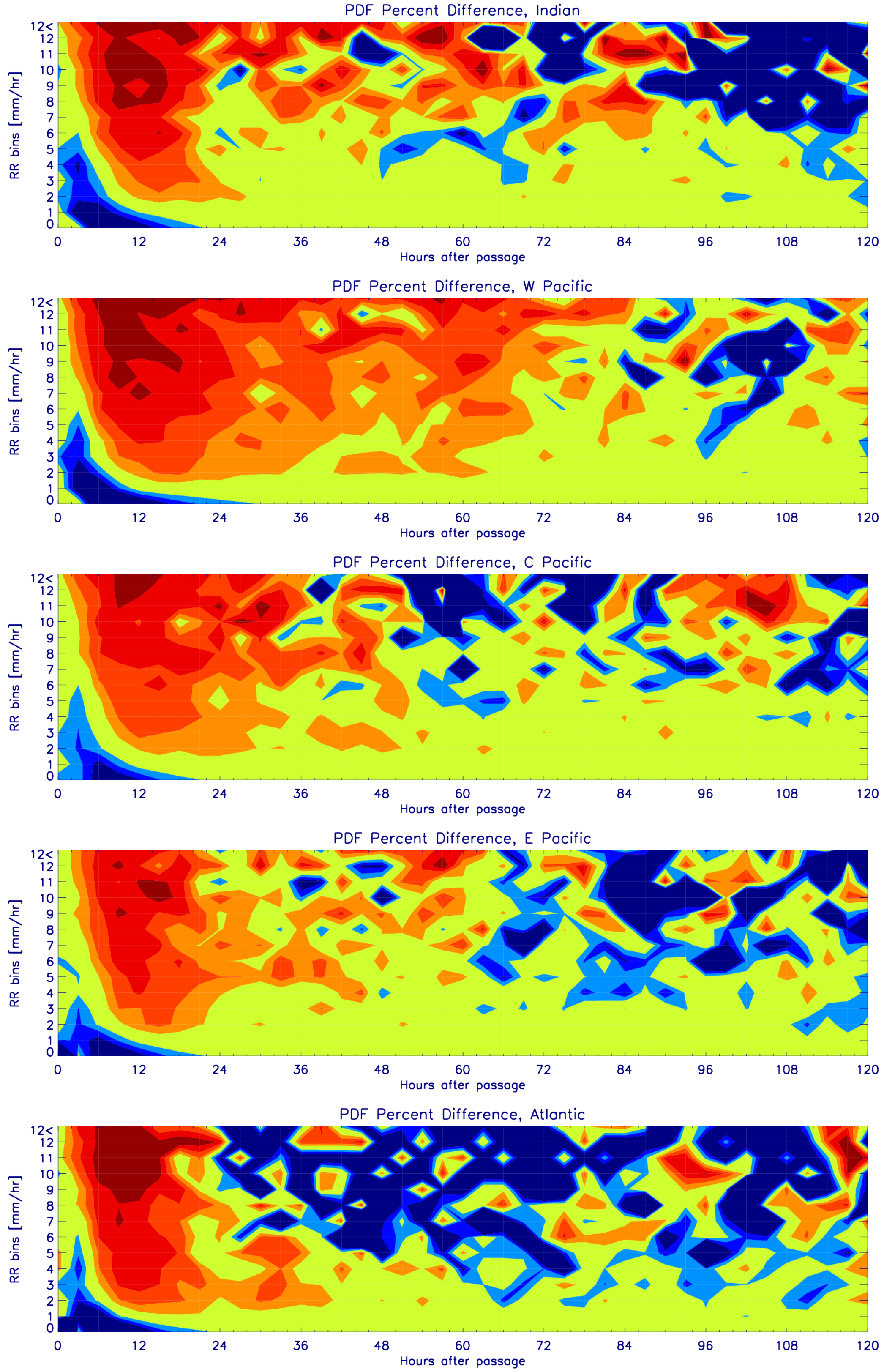

Figure 5.4. PDF percent differences separated by basin. Contours follow the method of Figure 5.3.

To conclude, there is not a clear short-term feedback on rainfall that is related to MCS speed. Inter-basin variability, the influence of large-scale weather structures like the MJO and tropical cyclones, and the importance of tropical wave dynamics all make it very difficult to ascribe small differences in the PDFs of rain rates for fast and slow systems to the environmental impacts detailed in Section 4. It is possible that large-scale dynamics would dwarf any effect that a slightly depressed SST could have on local rainfall distributions, rendering the signal very small. So, while it may be possible to filter the input data in such a way to tease out certain small feedbacks, they are not readily apparent in the analysis performed.

6. SUMMARY

6.1 Summary

Heavily raining systems in the Tropical Ocean have been objectively categorized, tracked, and analyzed for their effects on local water and energy budgets. Tracked systems are coincident with deep clouds, large-scale water vapor convergence, increased columnar water vapor, greatly decreased net surface radiation, and decreasing sea surface temperatures. Despite the general consistency of system characteristics among ocean basins, the environmental effects caused by the passage of a heavily raining MCS show a dependence on basin and also a dependence on the propagation speed of systems. Different system speeds cause slightly different environmental effects due to the residence time of the cloud system and presumably being driven by different atmospheric dynamics, as evidenced by wind shear profiles. The witnessed decrease in SSTs prompted the exploration of rain rate feedbacks due to differing system speeds, with no clear feedback found in the analysis performed.

The methods for tracking and categorizing systems provided interesting results and possible frameworks for future work. Output from the methods used yield results that are broadly similar to others in the scientific literature, but also show certain advantages over alternative methods. A majority of tropical rainfall accumulation comes from deep convective cloud systems, propagating systems often move to the west and move at faster speeds than eastward propagating systems, and there is no net effect on TPW due to the passage of a MCS—all are findings corroborated by studies which use other methods. The propagation characteristics of tracked systems are remarkably similar among ocean basins. This is an important result given that most studies that employ tracking methods focus on smaller domains. This study's heavy reliance on satellite-derived data products demonstrates their utility in combined analyses of atmospheric phenomena, aiding to shrink the gap between the study of weather and climate; however, difficulties such as those encountered with using interpolated SST data are a reminder that every observational dataset has its limitations.

Environments in the Tropical Ocean affected by deep convective tropical raining systems, using the definition given in this study, witnessed a decrease in SST of 0.1-0.3°C and an increase in TPW of 5-7kg/m^2 that is mostly due to moistening between 850mb and 500mb. Large-scale water vapor convergence and a deep, optically thick cloud field are typically associated with the tracked systems. The decrease in SST is almost entirely due to the sharp decrease in the net surface radiative flux, caused by the pervasive, optically thick cloud field of the precipitating system. The use of a Lagrangian approach, following systems as they moved in time and space, allowed for detailed analysis of cloud properties and various components of the water and energy budgets of many locations.

REFERENCES

Adler, R. F., and Coauthors, 2003: The Version-2 Global Precipitation Climatology Project (GPCP) monthly precipitation analysis (1979–Present). *J. Hydrometeorology.* **4**, 1147-1167.

Adler, R. F., G. Gu, and G. J. Huffman, 2012: Estimating climatological bias errors for the Global Precipitation Climatology Project (GPCP). *J. Appl. Meteorol. and Climatology*, **51**, 84-99.

Anderberg, M. R., 1973: *Cluster analysis for applications*. Academic Press, 359 pp.

Arkin, P. A., and P. E. Ardanuy, 1989: Estimating climatic-scale precipitation from space: a review. *J. Climate*, **2**, 1229–1238.

Berg, W., T. S. L'Ecuyer, and C. D. Kummerow, 2006: Rainfall climate regimes: the relationship of regional TRMM rainfall biases to the environment. *J. of Appl. Meteorol. and Climatol.*, **45**, 434-454.

Bogdanoff, A. S. and C. A. Clayson, 2013: Estimation of sea surface diurnal warming. *J. Phys. Oceanogr*. (In preparation).

Cayan, D. R., 1992: Variability of latent and sensible heat fluxes estimated using bulk formulae. *Atmosphere-Ocean*, **30**, 1-42.

Chelton, D. B. and F. J. Wentz, 2005: Global microwave satellite observations of sea surface temperature for numerical weather prediction and climate research, *Bull. Amer. Meteor. Soc.*, **86**, 1097-1115.

Clayson, C. A., J. B. Roberts, and A. S. Bogdanoff, 2013: SeaFlux turbulent flux data set. *Bull. Amer. Meteor. Soc.* (In preparation).

de Boyer Montégut, C., G. Madec, A. S. Fischer, A. Lazar, and D. Iudicone, 2004: Mixed layer depth over the global ocean: An examination of profile data and a profile-based climatology, *J. Geophys. Res.*, **109**, C12003, doi:10.1029/2004JC002378.

Dee, D.P., and Coauthors, 2011: The ERA-Interim reanalysis: configuration and performance of the data assimilation system. *Q. J. R. Meteorol. Soc.* 137, 553–597. DOI:10.1002/qj.828

Dias, J., S. Tulich, and G. Kiladis, 2012: An object-based approach to assessing tropical convection organization. *J. Atmos. Sci.*, **69**, 2488-2504.

Elsaesser, G. S., C. D. Kummerow, T. S. L'Ecuyer, Y. N. Takayabu, and S. Shige, 2010: Observed self-similarity of precipitation regimes over the tropical oceans. *J. Climate*, **23**, 2686-2698.

Freitag, H. P., M. E. McCarty, C. Nosse, R. Lukas, M. J. McPhaden, and M. F. Cronin, 1999: COARE Seacat data: Calibrations and quality control procedures. NOAA Tech. Memo. ERL PMEL-115, 89 pp.

Gu, G., R. F. Adler, G. J. Huffman, and S. Curtis, 2007: Tropical rainfall variability on interannual-to-interdecadal and longer time scales derived from the GPCP monthly product. *J. Climate*, **20**, 4033-4046.

Gosnell, R., C. Fairall and P. J. Webster, 1995: The sensible heat of rainfall in the tropical ocean. *J. Geophys. Res.*, **100**, 18437-18442.

Held, I. M., and B. J. Soden, 2006: Robust responses of the hydrological cycle to global warming. *J. Climate*, **19**, 5686-5699.

Houze, R. A., 1989: Observed structure of mesoscale convective systems and implications for large-scale heating. *Q. J. R. Meteorol. Soc.*, **115**, 425-461.

Hsu, K., X. Gao, S. Sorooshian, and H. V. Gupta, 1997: Precipitation estimation from remotely sensed information using artificial neural networks. *J. Appl. Meteor.*, **36**, 1176–1190.

Huffman, G. J., and Coauthors, 2007: The TRMM Multisatellite Precipitation Analysis (TMPA): Quasi-global, multiyear, combined-sensor precipitation estimates at fine scales. *J. Hydrometeor.*, **8**, 38-55.

Jakob, C., and G. Tselioudis, 2003: Objective identification of cloud regimes in the tropical Western Pacific. *Geophys. Res. Lett.*, **30**, 2082, doi:10.1029/2003GL018367.

Jakob, C. and C. Schumacher, 2008: Precipitation and latent heating characteristic of the major tropical western pacific cloud regimes. *J. Climate*, **21**, 4348-4364.

Johnson, R. H., T. M. Rickenbach, S. A. Rutledge, P. E. Ciesielski, and W. H. Schubert, 1999: Trimodal characteristics of tropical convection. *J. Climate*, **12**, 2397-2418.

Joyce, R. J., J. E. Janowiak, P. A. Arkin, and P. Xie, 2004: CMORPH: A method that produces global precipitation estimates from passive microwave and infrared data at high spatial and temporal resolution. *J. Hydrometeorology*, **5**, 487-503.

Katsaros, K. B., and K. J. K. Buettner, 1969: Influence of rainfall on temperature and salinity of the ocean surface. *J. Appl. Meteorol.*, **8**, 15-18.

Kawai, Y. and A. Wada, 2007: Diurnal sea surface temperature variation and its impact on the atmosphere and ocean: a review. *J. Oceanography*, **63**, 721-744.

Kikuchi, K. and B. Wang, 2008: Diurnal precipitation regimes in the global tropics. *J. Climate*, **21**, 2680-2696.

Kummerow, C. D., W. S. Olson, and L. Giglio, 1996: A simplified scheme for obtaining precipitation and vertical hydrometeor profiles from passive microwave sensors. *IEEE Transactions on Geoscience and Remote Sensing*, **34**, 1213-1232.

Kummerow, C. D., W. Barnes, T. Kozu, J. Shiue, and J. Simpson, 1998: The Tropical Rainfall Measuring Mission (TRMM) sensor package. *J. Atmos. and Oceanic Tech.*, **15**, 809-817.

Kummerow, C. D., and Coauthors, 2000: The Status of the Tropical Rainfall Measuring Mission (TRMM) after two years in orbit. *J. Appl. Meteorol.* **39**, 1965-1982.

Kummerow, C. D., W. Berg, J. Thomas-Stahle, and H. Masunaga, 2006: Quantifying global uncertainties in a simple microwave rainfall algorithm, *J. Atmos. Oceanic Tech.*, **23**, 23-37.

Kummerow, C. D., S. Ringerud, J. Crook, D. Randel and W. Berg, 2011: An observationally generated a-priori database for microwave rainfall retrievals, *J. Atmos. and Oceanic Tech.*, **28**, 113-130, doi: 10.1175/2010JTECHA1468.1.

Lau, K.-M., and H.-T. Wu, 2011: Climatology and changes in tropical oceanic rainfall characteristics inferred from Tropical Rainfall Measuring Mission (TRMM) data (1998–2009). *J. Geophys. Research.*, **116**, D17111, doi:10.1029/2011JD015827.

Lee, D., L. Oreopoulos, G. Huffman, W. Rossow, and I. Kang, 2013: The precipitation characteristics of ISCCP tropical weather states. *J. Climate.* **26**, 772-788.

Li, Y., and R. E. Carbone, 2012: Excitation of rainfall over the Tropical Western Pacific. *J. Atmos. Sci.*, **69**, 2983-2994.

Madden, R. A., and P. R. Julian, 1972: Description of global-scale circulation cells in the tropics with a 40-50 day period. *J. Atmos. Sci.*, **29**, 1109-1123.

Mapes, B., S. Tulich, J. Lin, and P. Zuidema, 2006: The mesoscale convection life-cycle: Building block or prototype for large-scale tropical waves? *Dyn. Atmos. Oceans*, **42**, 3–29.

Masunaga, H., 2012: A satellite study of the atmospheric forcing and response to moist convection over tropical and subtropical oceans. *J. Atmos. Sci.*, **69**, 150-167.

McPhaden, M.J., K. Ando, B. Bourlès, H.P. Freitag, R. Lumpkin, Y. Masumoto, V.S.N. Murty, P. Nobre, M. Ravichandran, J. Vialard, D. Vousden, and W. Yu, 2010: The global tropical moored buoy array. In *Proceedings of the "Ocean Obs '09: Sustained Ocean Observations and Information for Society" Conference (Vol. 2)*, Venice, Italy, 21–25 September 2009, Hall, J., D.E. Harrison, and D. Stammer, Eds., ESA Publication WPP-306.

Meehl, G.A., and Coauthors, 2007: Global climate projections. *Climate Change 2007: The Physical Science Basis*. Cambridge University Press, 881 pp.

Mohr, K. I., J. S. Famiglietti, and E. J. Zipser, 1999: The contribution to tropical rainfall with respect to convective system type, size, and intensity estimated from the ice scattering signature. *J. Appl. Meteorol.*, **38**, 596-606.

Peixoto, J. P., and A. H. Oort, 1992: *Physics of Climate*. American Institute of Physics, 1992. 520 pp.

Reynolds, R. W., T. Smith, C. Liu, D. Chelton, K. Casey, and M. Schlax, 2007: Daily high-resolution-blended analyses for sea surface temperature. *J. Climate*, **20**, 5473-5496.

Rossow, W. B., and R. A. Schiffer, 1999: Advances in understanding clouds from ISCCP. *Bull. Amer. Meteorol. Soc.*, **80**, 2261-2288.

Rossow, W. B., G. Tselioudis, A. Polak, and C. Jakob, 2005: Tropical climate described as a distribution of weather states indicated by distinct mesoscale cloud property mixtures. *Geophys. Res. Lett.,* **32**, doi:10.1029/2005GL024584.

Rossow, W. B. A. Mekonnen, C. Pearl, and W. Goncalves, 2012: Tropical precipitation extremes. *J. Climate*, in review.

Sapiano, M. R. P., and P. A. Arkin, 2009: An intercomparison and validation of high-resolution satellite precipitation estimates with 3-hourly gauge data. *J. Hydrometeorology*, **10**, 149-166.

Schrage, J. M., C. A. Clayson, 2003: Precipitation and freshwater lens formation in the Tropical Western Pacific. First Conference in Observing and Understanding Variability of Water in Weather and Climate, American Meteorological Society, Boston MA.

Skok, G., J. Tribbia, J. Rakovec, and B. Brown, 2009: Object-based analysis of satellite-derived precipitation systems over the low- and mid-latitude Pacific Ocean. *Mon. Wea. Rev.*, **137**, 3196–3218.

Soden, Brian J., 2000: The sensitivity of the tropical hydrological cycle to ENSO. *J. Climate*, **13**, 538-549.

Stackhouse, Jr., P. W., S. Gupta, S. Cox, J. Mikovitz, T. Zhang, and L. Hinkelman, 2011: The NASA/GEWEX Surface Radiation Budget release 3.0: 24.5-year dataset. *GEWEX News,* 21, Feb., 10-12.

Stephens, G. L., P. J. Webster, R. H. Johnson, R. Engelen, and T. S. L'Ecuyer, 2004: Observational evidence for the mutual regulation of the tropical hydrological cycle and tropical sea surface temperatures. *J. Climate*, **17**, 2213-2224.

Stephens, G. L., and C. D. Kummerow, 2007: The remote sensing of clouds and precipitation from space: A review. *J. Atmos. Sci.*, **64**, 3742-3765.

Stephens, G. L., T. L'Ecuyer, R. Forbes, A. Gettlemen, J.-C. Golaz, A. Bodas-Salcedo, K. Suzuki, P. Gabriel, and J. Haynes, 2010: Dreary state of precipitation in global models. *J. Geophys. Res.,* **115**, D24211, doi:10.1029/2010JD014532.

Stephens, G. L., and Coauthors, 2012: An update on Earth's energy balance in light of the latest global observations. *Nature Geoscience*, **5**, 691-696. doi: 10.1038/NGEO1580

Trenberth, K. E., 1997: The definition of El Niño. *Bull. Amer. Meteor. Soc.*, **78**, 2771–2777.

Trenberth, K. E., J. T. Fasullo, and J. Kiehl, 2009: Earth's global energy budget. *Bull. Amer. Meteorol. Soc.*, **90**, 311-323.

Tulich, S., and G. Kiladis, 2012: Squall lines and convectively coupled gravity waves in the tropics: Why do most cloud systems propagate westward? *J. Atmos. Sci.*, **69**, 2995-3012.

Webster, P. J., and R. Lukas, 1992: TOGA-COARE: The coupled ocean-atmosphere experiment. *Bull. Amer. Meteor. Soc.*, **73**, 1377-1416.

Wentz, F. J., L. Ricciardulli, K. Hilburn, and C. Mears, 2007: How much more rain will global warming bring? *Science*, **317**, 233-235.

Wheeler, M., and G. N. Kiladis, 1999: Convectively coupled equatorial waves: analysis of clouds and temperature in the wavenumber–frequency domain. *J. Atmos. Sci.,* **56**, 374-399.

Wild, M., 2012: New directions: a facelift for the picture of the global energy balance. *Atmos. Enviro.* **55**, 366-367.

APPENDIX

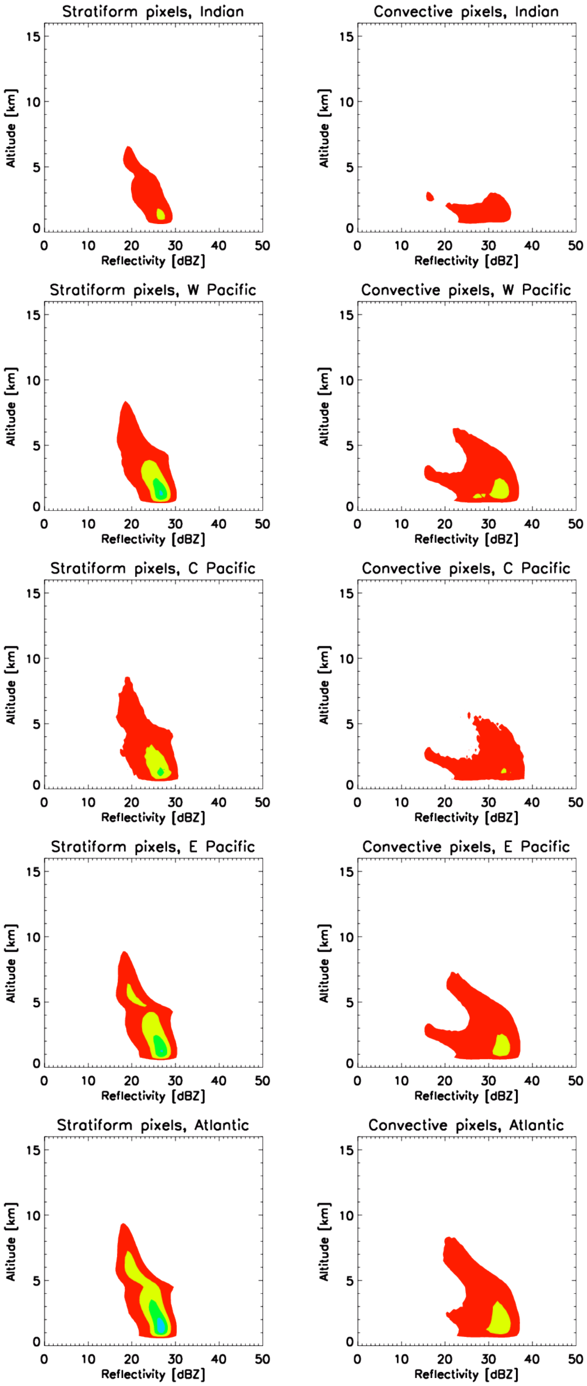

Figure A.1. CFADs of radar reflectivity for the TMI-derived shallow precipitating regime separated by basin (rows) and convective (right) versus stratiform (left) pixels.

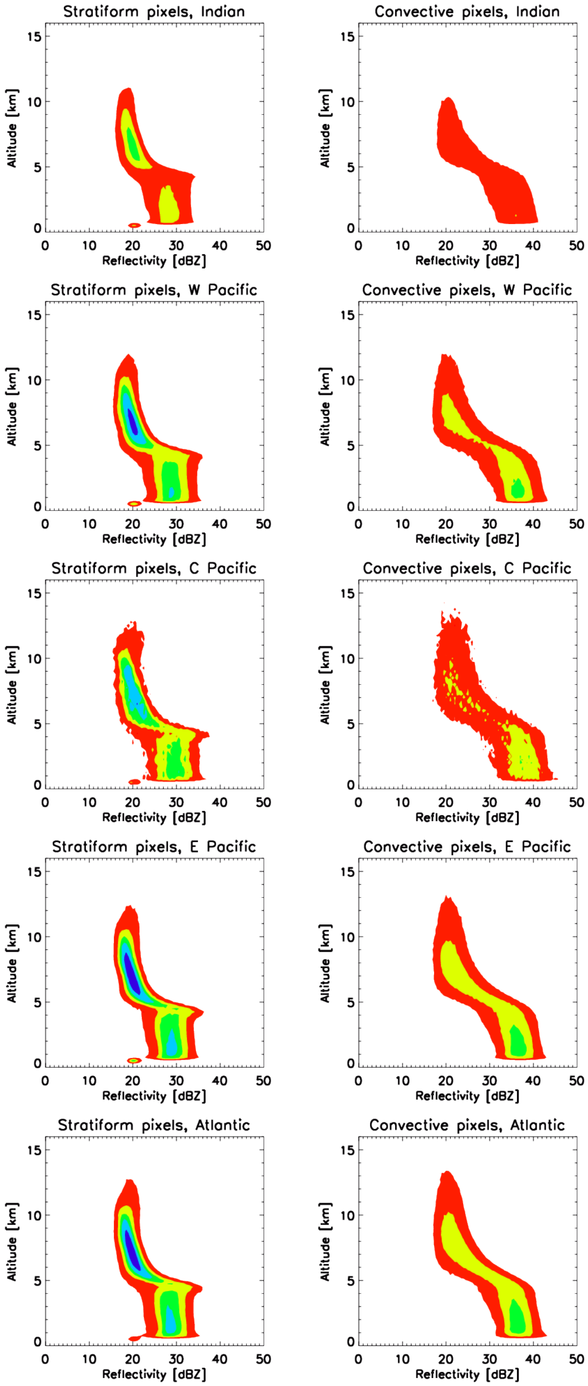

Figure A.2. CFADs of radar reflectivity for the TMI-derived unorganized convective precipitating regime separated by basin (rows) and convective (right) versus stratiform (left) pixels.

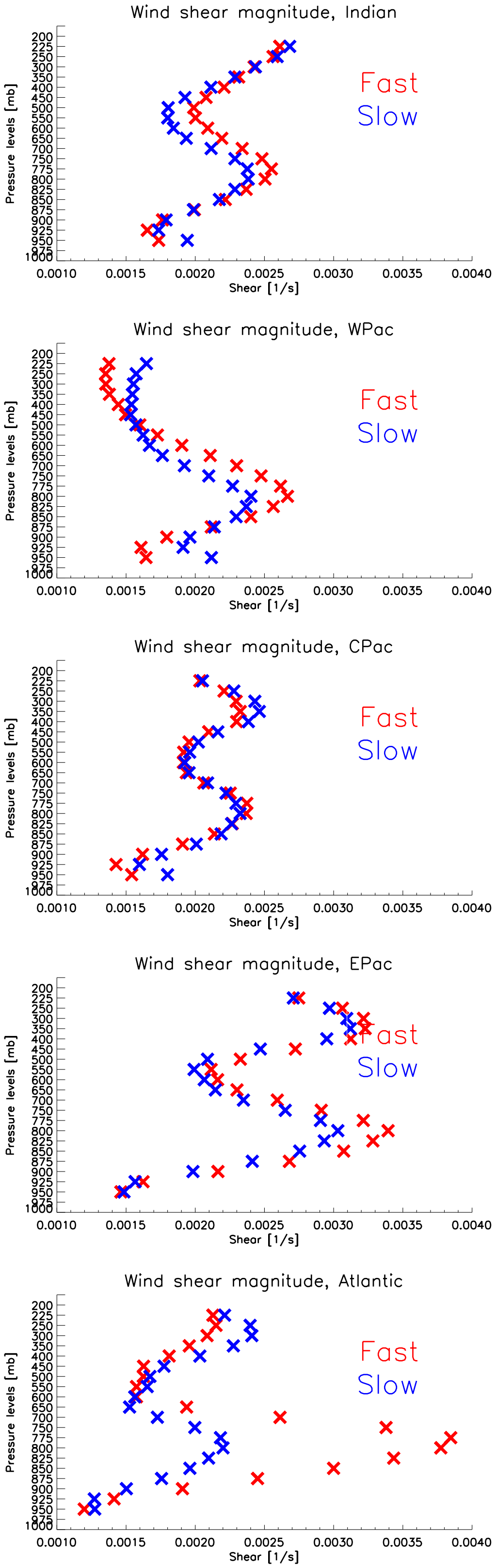

Figure A.3. Wind shear profiles by basin, with *lev*=2 (defined in section 2.4.2).

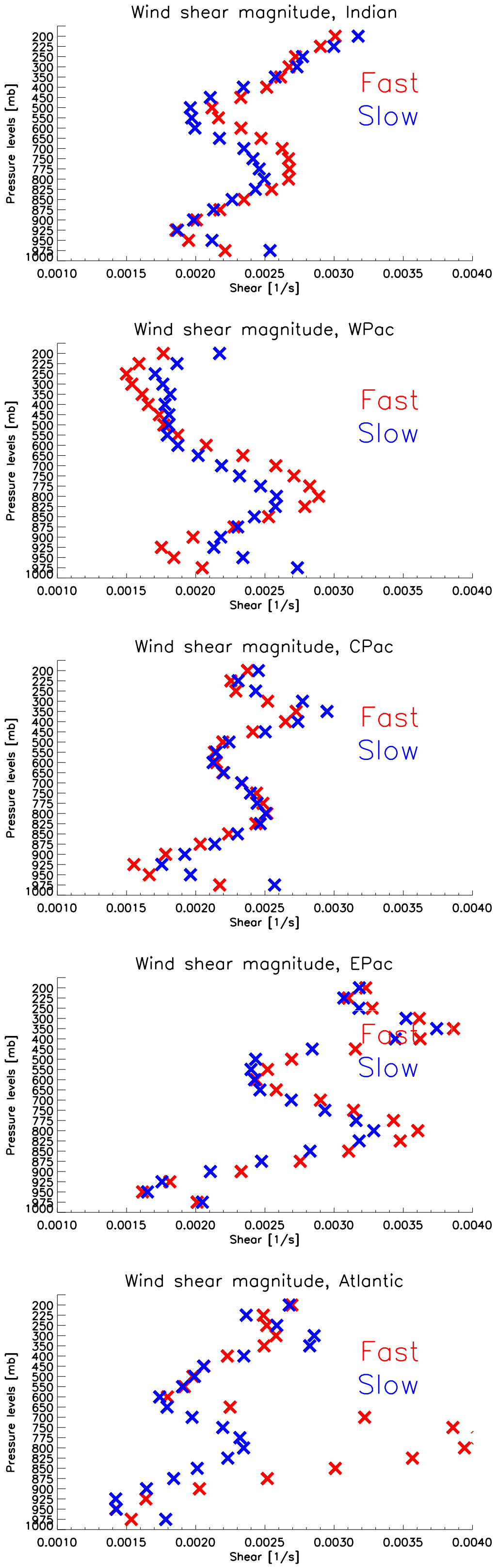

Figure A.4. Wind shear profiles by basin, with *lev*=1 (defined in section 2.4.2).

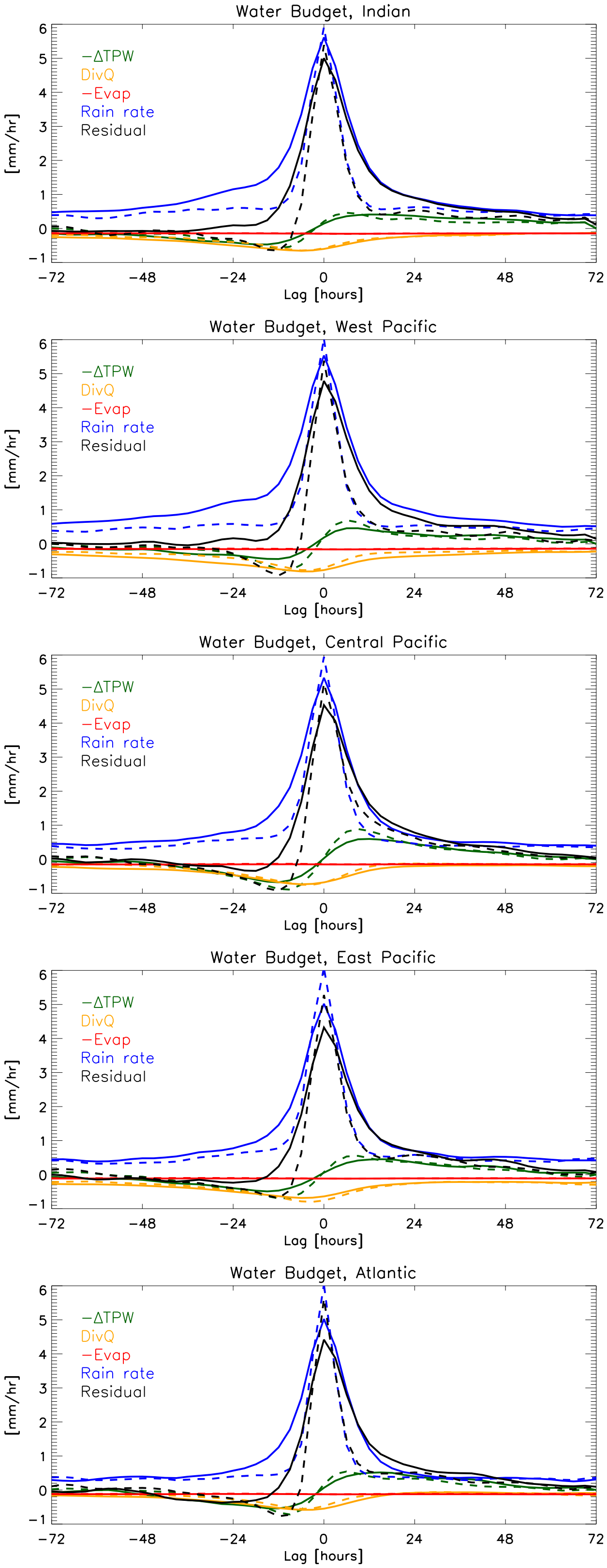

Figure A.5. Water budget analysis separated by basin (compare to Figure 4.9).

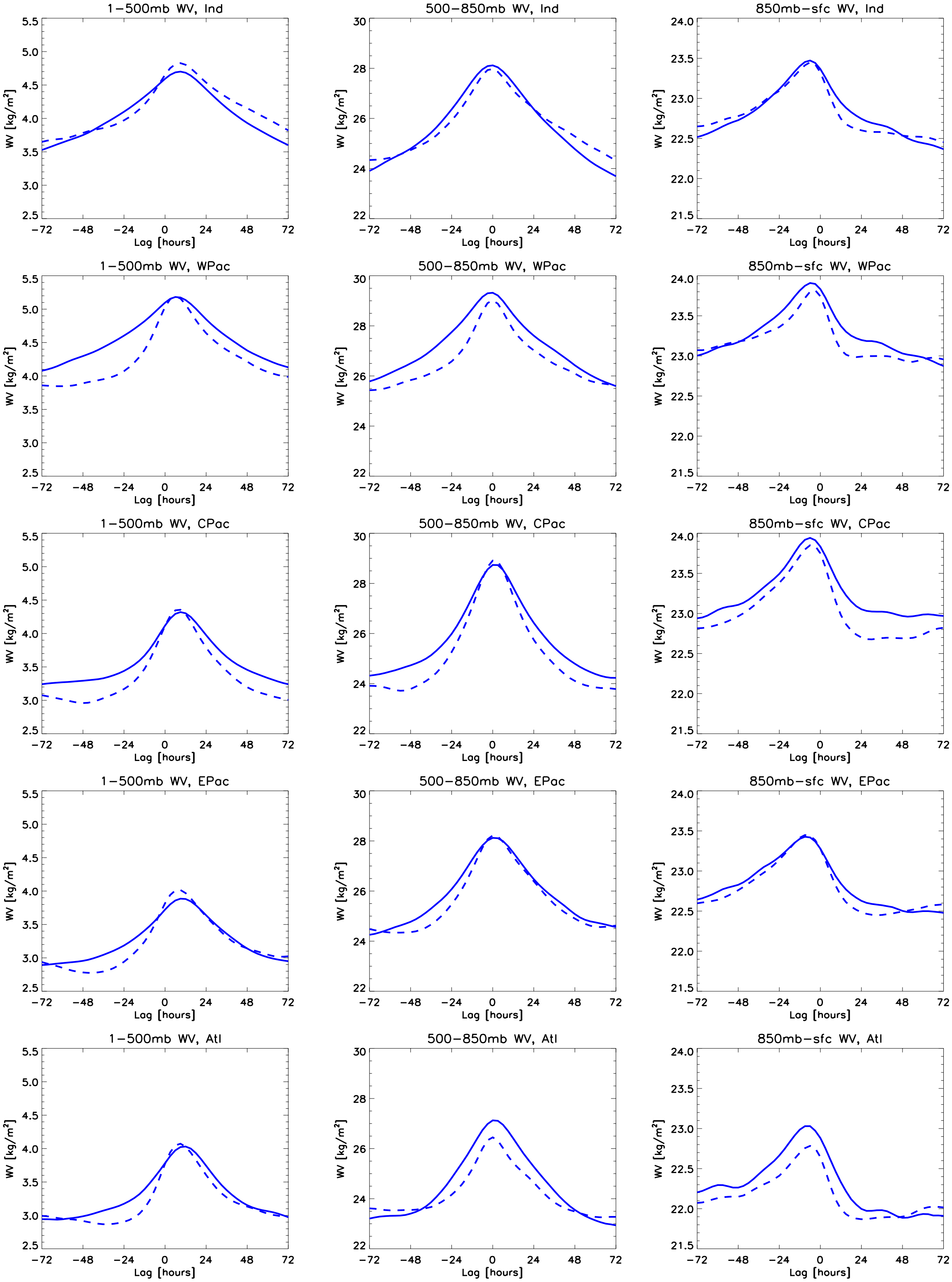

Figure A.6. Changes in water vapor for three intervals, separated by ocean basin, for fast (dashed) and slow (solid) systems.

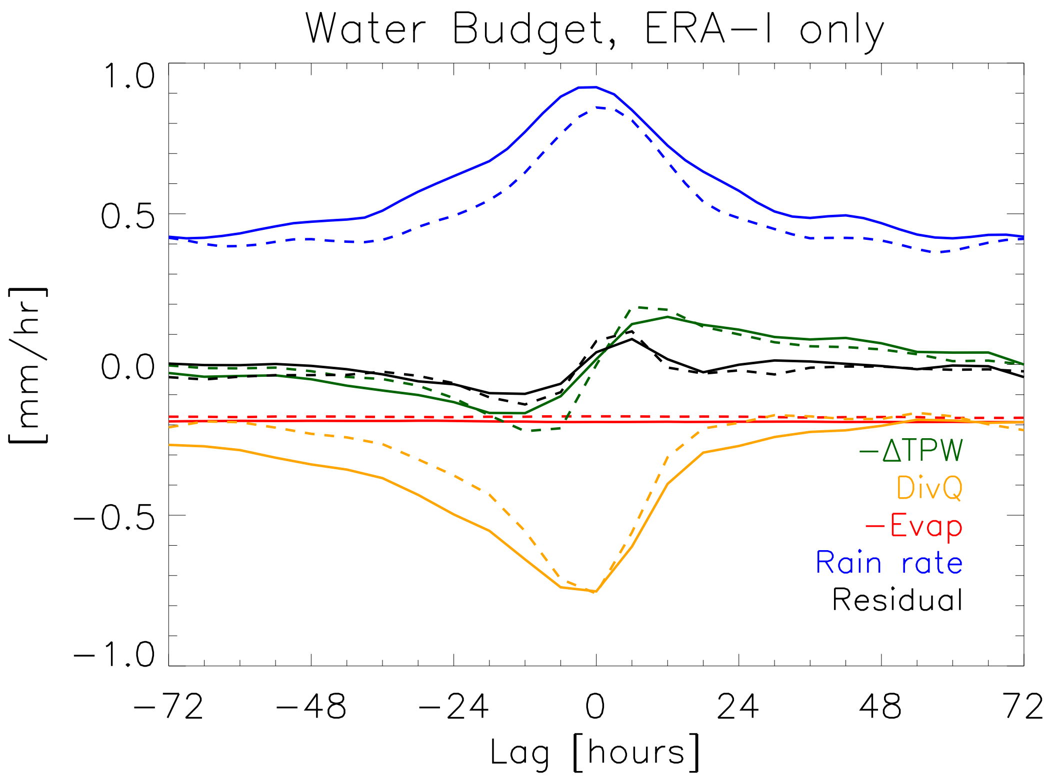

Figure A.7. Same as in Figure 4.9 but using ERA-Interim products exclusively.

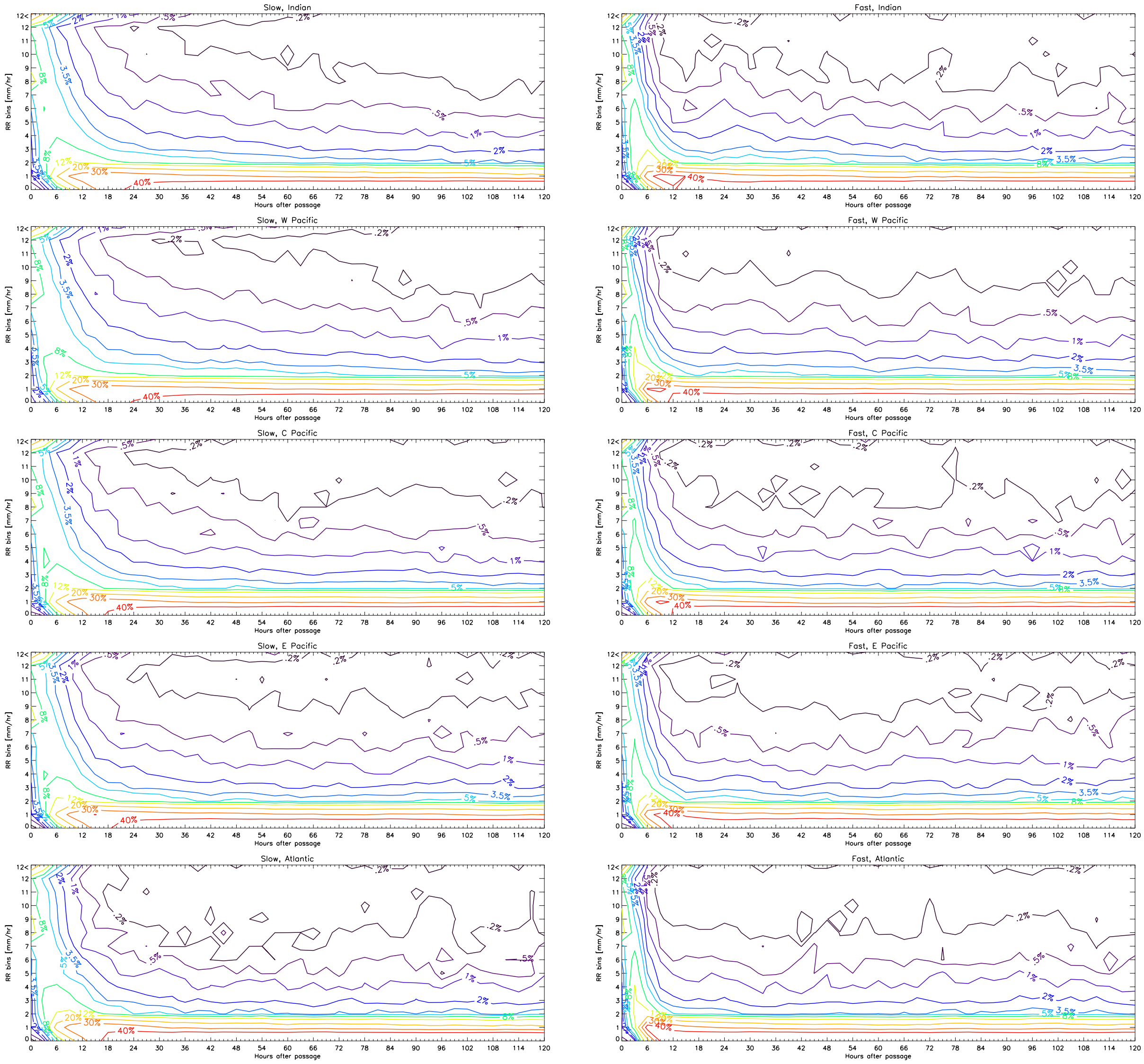

Slow, Indian

Fast, Indian

Slow, W Pacific

Fast, W Pacific

Slow, C Pacific

Fast, C Pacific

Slow, E Pacific

Fast, E Pacific

Slow, Atlantic

Fast, Atlantic

Figure A.8. As in Figure 5.1, for 5 days and separated by basin with Slow (left) and Fast (right) systems.